



**University of  
Zurich<sup>UZH</sup>**

# Sensitivity Study of Heavy Neutrino Searches at the LHCb Experiment

Master Thesis in Physics

**Maryam Mourad**

Supervised by  
Prof. Nicola Serra  
Dr. Patrick Owen  
Dr. Gerardo Vasquez

February 6, 2025





## **Abstract**

Heavy neutrinos are beyond the Standard Model particles which could be responsible for providing mass to the Standard Model neutrinos. In this thesis, I start with a theoretical review of the Standard Model, neutrino oscillations, and a mechanism to provide mass to neutrinos in presence of heavier counterparts. I then review some of the best searches for heavy neutrinos in a wide range of mass, and motivate a search in decays of the B mesons recorded by the LHCb experiment. Finally, I present my analysis of the sensitivity of LHCb to heavy neutrinos in the LHC Run3 and HL-LHC. Following a thorough study of the signal selection and acceptance, I present the resulting expected number of heavy neutrino events per year, for both Dirac and Majorana heavy neutrinos and for various mass points.

### **Acknowledgements**

To my parents for always believing in me and supporting me unconditionally. To Lukas, Asmaa, and Arash, for always being there, for your endless support, trust, and encouragement, and for making this journey a wonderful one. I couldn't have done this without you by my side. I also want to thank myself, for not giving up, even when things felt impossible, being kind to myself when I needed a break, believing in myself, and trusting that I could make it here.

# Contents

<b>1</b>	<b>Introduction</b>	<b>1</b>
<b>2</b>	<b>The Standard Model of Particle Physics</b>	<b>2</b>
2.1	Introduction . . . . .	2
2.2	Standard Model Lagrangian . . . . .	3
2.2.1	Gauge Sector . . . . .	3
2.2.2	Fermion Sector . . . . .	4
2.2.3	Higgs Sector . . . . .	4
2.2.4	Yukawa Interactions . . . . .	4
<b>3</b>	<b>Heavy Neutrino</b>	<b>6</b>
3.1	Neutrino oscillation . . . . .	6
3.2	Neutrino mass . . . . .	7
3.3	Previous experimental searches . . . . .	10
3.3.1	Search for heavy neutrinos at the LHCb experiment in $B^- \rightarrow \pi^+ \mu^- \mu^-$ . .	11
3.4	Proposed search in $B_c$ decays . . . . .	15
<b>4</b>	<b>The LHCb experiment</b>	<b>18</b>
4.1	The Large Hadron Collider . . . . .	18
4.2	The LHCb Experiment . . . . .	19
<b>5</b>	<b>Sensitivity of the LHCb experiment in heavy neutrino searches</b>	<b>21</b>
5.1	Introduction . . . . .	21
5.2	Signal and background processes . . . . .	21
5.3	Monte Carlo simulation . . . . .	22
5.4	Kinematics of signal and background processes . . . . .	24
5.5	Acceptance and efficiency . . . . .	31
5.5.1	Trigger and geometrical acceptance . . . . .	31
5.5.2	$J/\psi$ background reduction . . . . .	32
5.5.3	Flight distance selections . . . . .	32
5.6	Results . . . . .	35
5.6.1	Lepton number violating process . . . . .	35
5.6.2	Sensitivity to Majorana and Dirac heavy neutrinos . . . . .	37
<b>6</b>	<b>Summary and conclusion</b>	<b>43</b>

# 1 Introduction

The Standard Model (SM) of particle physics is the current best theory to describe the building blocks of the universe and their interactions. While this theory has been remarkably successful, it faces both theoretical and experimental challenges, hinting on physics beyond the Standard Model with new elementary particles.

The SM can be extended by adding one or a few particles beyond the SM, called *heavy neutrinos* (HN). While neutrinos in SM are three massless leptons, experimental observation of their oscillation shows that at least two of them should have a mass. The addition of HN allows for a natural and minimal mechanism to add mass to SM neutrinos, while providing beyond-SM dark matter candidates.

Following a brief review of the SM in chapter 2, I introduce HNs in chapter 3, the need for them, the mechanism to provide mass to SM neutrinos, and review the current best searches. A particular focus will be on the searches in decays of the B mesons, including a proposal for such a search in the LHCb experiment, which is explained in chapter 4.

In chapter 5, I present my analysis on the sensitivity of the LHCb experiment in the search for HN candidates in decays of  $B_c$  mesons. This includes a detailed study of the kinematics of this process for various HN candidates with different masses, a study of most prominent background processes, their kinematics, and their reduction methods, a detailed study of detector acceptance and efficiency factors, and finally the results of the analysis represented by the number of potential HN observed events per year, for given HN mass, its coupling to SM leptons, and its Dirac or Majorana nature.

# 2 The Standard Model of Particle Physics

## 2.1 Introduction

The Standard Model (SM) of particle physics is the most successful theory in describing the elementary particles of our universe: quarks, leptons, and gauge bosons and their interactions. It unifies all known forces except gravity, namely electromagnetic, weak, and strong forces, within the framework of quantum field theory. It is based on the gauge group:

$$SU(3)_C \times SU(2)_L \times U(1)_Y.$$

$SU(3)_C$  describes the strong force within quantum chromodynamics (QCD), while  $SU(2)_L$  and  $U(1)_Y$  together describe the electroweak force. After spontaneous symmetry breaking through the Higgs mechanism, the electroweak symmetry reduces to  $U(1)_{em}$ , corresponding to electromagnetism (QED) and the weak force.

The SM includes five fields whose quantum oscillations describe the particles we have observed in nature making up light matter. These fields differ from each other in the way they transform under the SM symmetry group. Table 2.1 shows the quantum numbers of each field under each subgroup of the SM.  $Q_L$  is the left-handed quark doublet, containing the up ( $u_L$ ) and down ( $d_L$ ) quarks,  $u_R$  is the right-handed up quark,  $d_R$  is the right-handed down quark,  $L_L$  is the left-handed lepton doublet, containing the electron ( $e_L$ ) and its neutrino ( $\nu_L$ ) and  $e_R$  is the right-handed electron.

		$SU(3)_c$	$SU(2)_L$	$U(1)_Y$
quarks	$Q_L$	3	2	+1/6
	$u_R$	3	1	+2/3
	$d_R$	3	1	-1/3
leptons	$L_L$	1	2	-1/2
	$e_R$	1	1	-1

Table 2.1: Transformation behaviour of the matter fields under the SM gauge group.

Naturally, one would want to include a right-handed neutrino field for completeness, but it has not yet been observed in nature. Each of these fields comes in three generations with identical properties under the gauge group but differing masses. Additionally, for each particle, there exists a corresponding antiparticle with the same mass but opposite quantum numbers.

The particles that mediate the interactions, the gauge bosons, are the following:

- **Gluons** ( $G_\mu^a$ ) (8, 1, 0) as gauge bosons of  $SU(3)_C$ . They mediate the strong interaction, carrying color charge.
- **Weak bosons** ( $W^\pm, W^3$ ) (1, 3, 0) as gauge bosons of  $SU(2)_L$ .  $W^\pm$  mediate the charged weak interactions.
- **Hypercharge boson** ( $B_\mu$ ) (1, 1, 0) as the gauge boson of  $U(1)_Y$ . It mixes with  $W^3$  after electroweak symmetry breaking to form  $\gamma$  and  $Z^0$ .

- **Photon** ( $\gamma$ ) (1, 1, 0) as the gauge boson of electromagnetism.
- **Z<sup>0</sup> boson** (1, 1, 0) which mediates neutral weak interactions.

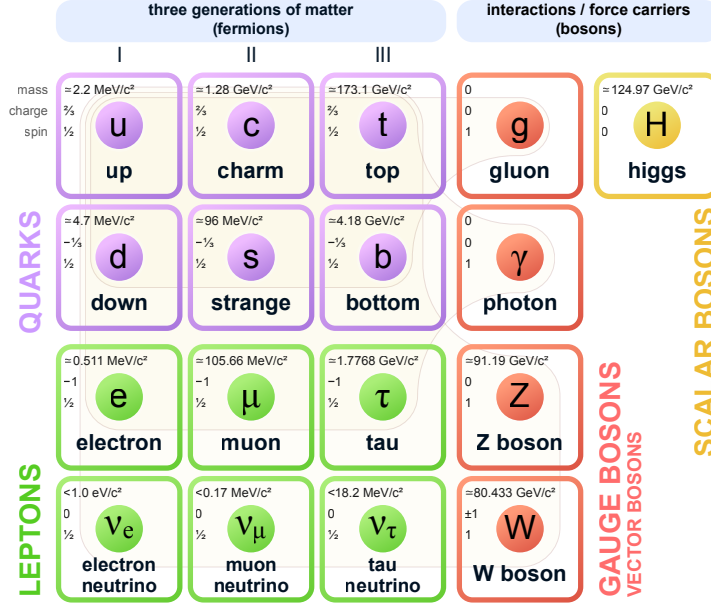


Figure 2.1: The particles of the Standard Model of particle physics and their properties. Figure is taken from reference [1].

## 2.2 Standard Model Lagrangian

The dynamics of all SM fields are described by the Lagrangian of the SM, which can be divided into several parts: the gauge sector, the fermion sector, the Higgs sector, and the Yukawa interactions. The full Lagrangian of the SM is expressed as:

$$\mathcal{L}_{\text{SM}} = \mathcal{L}_{\text{gauge}} + \mathcal{L}_{\text{fermion}} + \mathcal{L}_{\text{Higgs}} + \mathcal{L}_{\text{Yukawa}}.$$

$\mathcal{L}_{\text{gauge}}$  contains the Yang-Mills Lagrangian, which includes the kinetic terms for the gauge bosons and their self-interactions.  $\mathcal{L}_{\text{fermion}}$  includes the kinetic terms for fermions and their interactions with gauge bosons via covariant derivatives.  $\mathcal{L}_{\text{Higgs}}$  includes the kinetic term for the Higgs field and the Higgs potential, which is responsible for electroweak symmetry breaking. Finally,  $\mathcal{L}_{\text{Yukawa}}$  describes the interactions between the Higgs field and the fermions, generating fermion masses proportional to the Yukawa couplings after the Higgs field acquires a non-zero vacuum expectation value (VEV).

### 2.2.1 Gauge Sector

The gauge sector describes the kinetic terms and interactions of the gauge fields:

$$\mathcal{L}_{\text{gauge}} = -\frac{1}{4}G_{\mu\nu}^A G^{A\mu\nu} - \frac{1}{4}W_{\mu\nu}^a W^{a\mu\nu} - \frac{1}{4}B_{\mu\nu} B^{\mu\nu},$$

with  $\mu, \nu = 0, 1, 2, 3$ ,  $A = 1, \dots, 8$ ,  $a = 1, 2, 3$ , and  $G_{\mu\nu}^A$ ,  $W_{\mu\nu}^a$ , and  $B_{\mu\nu}$  the field strength tensors of  $SU(3)_C$ ,  $SU(2)_L$ , and  $U(1)_Y$ , respectively.

## 2.2.2 Fermion Sector

The fermion sector includes the kinetic terms for the quarks and leptons as well as their interactions with the gauge fields:

$$\mathcal{L}_{\text{fermion}} = \sum_{\text{generations}} [\bar{Q}_L i \not{D} Q_L + \bar{u}_R i \not{D} u_R + \bar{d}_R i \not{D} d_R + \bar{L}_L i \not{D} L_L + \bar{e}_R i \not{D} e_R],$$

where  $\not{D} = \gamma^\mu D_\mu$  is the Dirac operator  $\gamma^\mu$  coupled with the covariant derivative  $D_\mu$ :

$$D_\mu = \partial_\mu - ig_s G_\mu^A T^A - ig W_\mu^a \tau^a - ig' B_\mu Y,$$

where  $g_s$ ,  $g$ , and  $g'$  are the coupling constants for the strong, weak, and hypercharge interactions, respectively, and  $T^A$ ,  $\tau^a$ , and  $Y$  are the corresponding generators.

The gauge sector including the fermion sector has a global flavor symmetry, each of the five different fermion species can be rotated in flavor space with no consequences in gauge interactions.

## 2.2.3 Higgs Sector

The Higgs sector includes the kinetic term and potential for the Higgs field:

$$\mathcal{L}_{\text{Higgs}} = |D_\mu \Phi|^2 - V(\Phi),$$

where  $\Phi$  is the Higgs doublet and the potential  $V(\Phi)$  is given by:

$$V(\Phi) = \mu^2 |\Phi|^2 + \lambda |\Phi|^4,$$

where  $\mu^2 < 0$  gives a non-zero VEV for the Higgs field:

$$\langle \Phi \rangle = \left( v_H / \sqrt{2}, 0 \right)^T$$

This breaks the electroweak symmetry, leading to W and Z bosons acquiring mass while leaving the photon massless, thus separating the electromagnetic interaction from the weak force.

## 2.2.4 Yukawa Interactions

The interaction between the fermion fields with the Higgs fields, called the Yukawa interaction, breaks the flavor symmetry as it generates masses for the fermions via their couplings to the Higgs field:

$$\mathcal{L}_{\text{Yukawa}} = -y_u \bar{Q}_L \Phi u_R - y_d \bar{Q}_L \Phi d_R - y_e \bar{L}_L \Phi e_R + \text{h.c.},$$

where  $y_u$ ,  $y_d$ , and  $y_e$  are the Yukawa coupling constants for the up-type quarks, down-type quarks, and charged leptons, respectively. The Higgs field  $\Phi$  generates fermion masses after it acquires a VEV, such that the fermion masses are given by:

$$m_f = y_f \frac{v_H}{\sqrt{2}}.$$

### 2.2.4.1 Yukawa in the quark sector

In the quark sector, the flavors are not conserved. For each flavor generation, there are two terms in the Higgs-quark interaction Lagrangian. Hence, the Yukawa matrices cannot be simultaneously diagonalized leading to the misalignment of the mass eigenstates to the weak eigenstates of the quarks. This in turn impacts the gauge sector, resulting in the mixing of the quark families which is encapsulated in the Cabibbo-Kobayashi-Maskana (CKM) matrix  $V^{ij}$ ,  $i = u, c, t, j = d, s, b$ :

$$\mathcal{L}_W^{\text{int}} = \frac{g}{\sqrt{2}} \bar{q}_L^i V^{ij} \gamma^\mu q_L^j W_\mu^+ + \text{h.c.}$$

#### 2.2.4.2 Yukawa in the lepton sector

Due to the absence of the right-handed neutrino field, we only have one term in the SM Lagrangian for the interaction between the Higgs field and the leptons, which means that the Yukawa matrix can always be diagonalized, leading to the conservation of all three lepton flavors, thus our only physical parameters are the three lepton masses.

## 3 Heavy Neutrino

Despite its huge success, the SM faces theoretical and experimental challenges. It does not account for gravity, dark matter, dark energy or the matter-antimatter asymmetry in the universe to mention a few as well as experimental evidence that urge for extensions of the SM to be explored. One of the first experimental hints pointing towards physics beyond the SM was the discovery of neutrino oscillation [2, 3, 4]. Neutrino oscillation implies that neutrinos have non-zero mass, whereas neutrinos are postulated to be massless in the SM. Section 3.1 gives a brief introduction to neutrino oscillations based on references [5, 6]. Section 3.2 examines the mechanisms by which neutrinos can acquire mass through extensions of the SM, based on references [7, 6]. In section 3.3, I provide a summary of different strategies to search for heavy neutrinos (HN) and state some example experiments, as well as an overview over excluded regions for the mixing angles between light and HNs. In the final section 3.4, I will dive into an analysis which explores the detectability of HNs at LHCb via the decay  $B_c^+ \rightarrow \mu^+ \text{HN} \rightarrow \mu^+ \mu^+ \tau^- \bar{\nu}_\tau$ .

### 3.1 Neutrino oscillation

The theory of neutrino oscillation is similar to the mixing in the quark sector, as the neutrino mass eigenstates  $|\nu_1\rangle, |\nu_2\rangle$ , and  $|\nu_3\rangle$  are not the same as the flavour eigenstates  $|\nu_e\rangle, |\nu_\mu\rangle$ , and  $|\nu_\tau\rangle$ , but linear combinations of them:

$$|\nu_\ell\rangle = \sum_{i=1}^3 U_{\ell i} |\nu_i\rangle, \quad (3.1)$$

where  $\ell = e, \nu, \tau$  and  $\sum_{i=1}^3 U_{\ell i}$  are the matrix elements of the Pontecorvo-Maki-Nakagawa-Sakata (PMNS) matrix. Neutrinos interact as flavor eigenstates, but they propagate as eigenstates of the free-particle Hamiltonian. The same mixing happens with quarks, except that for them the familiar flavors (d, s, b) are the mass eigenstates, and the weak eigenstates (d', s', b') are rotated.

This implies that a neutrino of a specific flavor can be detected as a different flavor as it propagates through space, due to the mass eigenstates evolving with different phases. For a neutrino produced at time  $t = 0$  and detected at a later time  $t$ , the probability that a neutrino of flavor  $\alpha$  to be detected with a flavor  $\beta$  after traveling a distance  $L$  is given by:

$$P_{\alpha \rightarrow \beta} = \delta_{\alpha\beta} - 4 \sum_{i>j} \text{Re}(U_{\alpha i} U_{\beta j} U_{\alpha j}^* U_{\beta i}^*) \sin^2 \left( \frac{\Delta m_{ij}^2 L}{4E} \right) + 2 \sum_{i>j} \text{Im}(U_{\alpha i} U_{\beta j} U_{\alpha j}^* U_{\beta i}^*) \sin \left( \frac{\Delta m_{ij}^2 L}{2E} \right),$$

where  $\Delta m_{ij}^2 = m_i^2 - m_j^2$  are the mass-squared differences between the mass eigenstates,  $L$  is the distance travelled by the neutrino,  $E$  is the neutrino energy and  $U_{\alpha i}$  as before are the matrix elements of the PMNS matrix. The PMNS matrix describes the oscillation behavior, in absence of which, flavors are conserved.

The dependence on the mass-squared difference implies that in order for neutrino oscillations to exist, there must be a mixing in  $U$  and at least two of the neutrino masses must be different,

which in turn means that at least two of the  $\Delta m_{ij}^2$  must be non-zero, while the third neutrino mass eigenstate can remain massless. The mass-squared differences are typically denoted as:

$$\Delta_{21} = m_2^2 - m_1^2, \quad \Delta_{32} = m_3^2 - m_2^2, \quad \Delta_{31} = m_3^2 - m_1^2,$$

with the relation  $\Delta_{31} = \Delta_{21} + \Delta_{32}$ , leaving only two independent differences. The sign of  $\Delta m_{31}^2$  determines the ordering of the masses, which can be either *normal ordering* (NO) with  $m_1 < m_2 < m_3$  ( $\Delta m_{31}^2 > 0$ ) or *inverted ordering* (IO) with  $m_3 < m_1 < m_2$  ( $\Delta m_{31}^2 < 0$ ).

The first strong evidence for neutrino oscillations came from the study of solar neutrinos, where the observed flux of electron neutrinos from the Sun was found to be significantly lower than predictions and was solved theoretically by the mechanism of neutrino oscillations. This was later confirmed by many other experiments including the Sudbury Neutrino Observatory [3] and the Super-Kamiokande experiment, which also provided the first precise measurement for atmospheric neutrino oscillation [2]. A paper by Esteban et al. [8] conducts a comprehensive global analysis of neutrino oscillation data by combining results from long-baseline neutrino experiments such as T2K, NOvA, and KamLAND for measuring  $\Delta m_{21}^2$ , and from short-baseline neutrino experiments such as Daya Bay and RENO for measuring  $\Delta m_{3\ell}^2$ . They find the best fit values for the mass-squared splittings to be  $\Delta m_{21}^2 = 7.42_{-0.20}^{+0.21} \times 10^{-5} \text{eV}^2$  (NO),  $\Delta m_{31}^2 = +2.517_{-0.028}^{+0.026} \times 10^{-3} \text{eV}^2$  (NO), and  $\Delta m_{32}^2 = -2.498_{-0.028}^{+0.028} \times 10^{-3} \text{eV}^2$  (IO).

The measurements of neutrino oscillation provide the squared mass differences between neutrino mass eigenstates, but they do not give any information about the absolute masses, which remain unknown. Upper limits on neutrino masses were derived from cosmological considerations [9, 10], and several experiments attempting to measure the neutrino masses directly [11]. The upper limits on the SM neutrino masses are in the sub-eV range, which is much smaller than the masses of other SM particles. Furthermore, neutrino oscillation measurements do not provide any insight into the origin of neutrino masses. Subsection 3.2 will review possible mechanisms that can generate these extremely small neutrino masses.

## 3.2 Neutrino mass

In the SM there is no fundamental reason why neutrinos should have zero mass. However, to generate a mass term for the neutrinos, one has to extend the SM by introducing a right-handed Weyl spinor field  $\nu_R$ , which is a singlet under the SM gauge group and hence does not participate in the weak interactions. The left-handed neutrino ( $\nu_L$ ) is part of a  $SU(2)_L$  doublet under electroweak symmetry, represented as  $L = (\nu_L, \ell)$ , where  $\nu_L$  is a Weyl spinor. With the addition of the right-handed neutrino field, two types of mass terms can be written for neutrinos.

The first possibility is the Dirac mass term, similar to that for all charged fermions in the SM. This term couples the left-handed neutrino field ( $\nu_L$ ) to the right-handed neutrino field ( $\nu_R$ ). The Dirac mass term is written as

$$\mathcal{L}_{\text{Dirac}} = \bar{\nu} m_D \nu = \bar{\nu}_L m_D \nu_R + \text{h.c.}$$

This mass term can be generated after spontaneous symmetry breaking through the Higgs mechanism. The Higgs doublet  $\Phi$  couples to  $\nu_R$  and  $L$  through the Yukawa interaction:

$$\mathcal{L}_{\text{Yuk},\nu} = -\bar{L} y_\nu \cdot \tilde{\Phi} \nu_R + \text{h.c.}$$

where  $y_\nu$  is the Yukawa coupling for the neutrinos and  $\tilde{\Phi}$  is the conjugate of the Higgs doublet  $\tilde{\Phi} = i\sigma_2 \Phi^*$ . After electroweak symmetry breaking with  $\langle \tilde{\Phi} \rangle = (v_H/\sqrt{2}, 0)^T$ :

$$\mathcal{L}_{\text{Dirac}} = -\frac{v_H}{\sqrt{2}} \bar{\nu}_L y_\nu \nu_R + \text{h.c.}$$

where  $v_H$  is the vacuum expectation value (VEV) of the Higgs field and the Dirac mass is  $m_D \equiv y_\nu v_H / \sqrt{2}$ .

The Dirac mass term conserves lepton number, which is an accidental global symmetry of the SM and does not mirror any underlying fundamental symmetry. If this Lagrangian fully described neutrino masses, neutrinos would be Dirac particles, similar to quarks and charged leptons. However, to explain the observed smallness of neutrino masses, the Yukawa coupling  $y_\nu$  would need to be many orders of magnitude smaller than those of other SM fermions, motivating another mechanism.

As any neutral particle, neutrinos can in principle be either a Dirac or a Majorana particle. The charged fermions in the SM are Dirac particles, meaning that they are distinguishable from their charge-conjugated partners, their antiparticles. The second possibility of adding a mass term for the neutrinos is the Majorana mass term, which can only be written for particles that are their own antiparticles. The Majorana mass term takes the form:

$$\mathcal{L}_{\text{Majorana}} = -\frac{1}{2} \bar{\nu}^c M \nu,$$

where  $M$  is the Majorana mass,  $C$  is the charge-conjugation operator, and  $\nu^c = C\bar{\nu}^T$  is the charge-conjugate of  $\nu$ . This term involves a coupling between a neutrino field and its own charge-conjugate field, making the neutrino indistinguishable from its antiparticle. Consequently, Majorana neutrinos satisfy the condition:

$$\nu = \nu^c \equiv C\bar{\nu}^T,$$

where the bar indicates the Dirac adjoint:  $\bar{\nu} = \nu^\dagger \gamma^0$ . This reduces the degrees of freedom of the Lagrangian as  $\nu_L$  and  $\nu_R$  are not independent fields anymore but charge conjugates of each other. One can write a Majorana mass term for both left-handed and right-handed Weyl fields independently. A mass term involving only the left-handed neutrino, written as

$$\mathcal{L}_{\text{Majorana}, \nu_L} = \frac{1}{2} \nu_L^T C^\dagger M \nu_L + \text{h.c.},$$

is forbidden under the SM gauge group as it is not Lorentz covariant. On the other hand, it is allowed for  $\nu_R$  because it doesn't transform under the SM gauge group and therefore we can write a Majorana mass term for the  $\nu_R$  which is similarly:

$$\mathcal{L}_{\text{Majorana}, \nu_R} = \frac{1}{2} \nu_R^T C^\dagger M \nu_R + \text{h.c.},$$

where  $M$  denotes again the Majorana mass. This term violates lepton number conservation by two units  $\Delta L = 2$ .

The Majorana or Dirac nature of the neutrinos observed in nature is not yet known, and they may acquire mass through either mechanism. In principle, one has to include both allowed mass terms in the SM Lagrangian,  $\mathcal{L}_{\text{Dirac}}$  and  $\mathcal{L}_{\text{Majorana}, \nu_R}$ . Combining both mass terms in the Lagrangian we get:

$$\mathcal{L} = -\frac{1}{2} (\bar{\nu}_L, \bar{\nu}_R) \begin{pmatrix} 0 & m_D \\ m_D & M \end{pmatrix} \begin{pmatrix} \nu_L \\ \nu_R \end{pmatrix} + \text{h.c.},$$

where we assume for simplicity that we only have one left-handed neutrino field and one right-handed neutrino field. The two eigenstates of this mass matrix give us the two neutrino mass eigenstates, and the corresponding eigenvalues are the experimentally measurable masses of the two neutrinos. The combination of both mass terms violates lepton number conservation and, therefore, both neutrinos will behave as Majorana neutrinos. Now, when we include all three left-handed neutrino fields of the SM, we end up with the three light SM neutrinos and at

least one heavy Majorana neutrino, referred to as heavy neutral lepton (HNL) or simply heavy neutrino (HN). Heavy neutrino is a key concept in most models for the extension of the SM that account for the masses of the light neutrinos.

The mechanism that produces the observed very small masses of neutrinos is called *Type-1 Seesaw mechanism* [12, 13, 14, 15, 16], which assumes that  $m_D \ll M$ . In this case, we can approximate the Lagrangian as

$$\mathcal{L} \approx -\frac{1}{2}m_1\bar{\nu}_1\nu_1 - \frac{1}{2}m_2\bar{\nu}_2\nu_2 + \text{h.c.},$$

where  $m_1 = m_D^2/M$  and  $m_2 = M$ , representing the masses of the two Majorana neutrinos,  $\nu_1$  and  $\nu_2$ . The mass eigenstates of the new neutrinos can be written as:

$$\nu_1 \approx \nu_L - \frac{m_D}{M}\nu_R, \quad \nu_2 \approx \nu_R + \frac{m_D}{M}\nu_L.$$

The two neutrino fields don't have definite chirality anymore, but the left-handed (right-handed) component is heavily suppressed for  $\nu_2$  ( $\nu_1$ ). This fact makes the HN mass eigenstate mostly right-handed, making it very difficult to detect experimentally.

The Seesaw relation

$$m_\nu = \frac{v_H^2 y_\nu^2}{2 \cdot M}$$

presents the simplest form of the seesaw mechanism. There are two approaches to obtain small neutrino masses. Either through a large HN mass  $M$  or through a small Yukawa coupling. In some extensions of the model, an additional parameter can further suppress the masses via approximate symmetry considerations.

The parameter  $M$  is not dependent on the electroweak scale as it was not generated through the Higgs mechanism. Thus, the HN mass  $M$  can be taken to be very large, potentially reaching the Grand Unification scale  $\sim 10^{14}$  GeV. In this scenario, the suppression of neutrino masses is primarily due to the mass of its HN counterpart, eliminating the need for small Yukawa couplings. This results in a much smaller mass for one of the neutrinos, which explains the observed smallness of neutrino masses. However, such models are challenging to test directly, as the high scale of  $M$  is well beyond the reach of current experimental capabilities.

Another approach is to achieve small neutrino masses through small Yukawa couplings. In this case, the HN mass  $M$  can be significantly lower, allowing for HNs with masses in the GeV, MeV, or even eV range. This approach means that the HN can be probed in experiments as long as it still couples strongly enough to SM particles. These low-energy seesaw models have distinct experimental signatures that are highly dependent on the masses of the HNs and their mixing with the SM neutrinos. The degree of mixing between light and HNs is determined by the Yukawa coupling strengths and the masses of the HNs. A short discussion about experimental signatures of these HNs and current constraints is provided in section 3.3.

The seesaw mechanism does not define a specific number of electroweak-singlet neutrinos, nor does it inherently favor high-energy or low-energy seesaw scales. The experimental evidence also does not offer a clear indication of which scale is more likely, but only the low-energy models offer HN candidates that can be probed in the current or near-future experiments. These models motivate and provide a framework for my analysis described in chapter 5.

Certain low-energy seesaw-type models not only offer an explanation for the smallness of neutrino masses, but can also offer dark matter candidates [17, 18] and a framework to explain the matter-antimatter asymmetry in the universe [19]. One prominent example is the Neutrino Minimal Standard Model ( $\nu$ MSSM). The  $\nu$ MSSM [20, 21], is a minimal extension of the SM that adds three right-handed neutrinos ( $N_1, N_2, N_3$ ). It can account for beyond-SM evidence while requiring minimal new particles or interactions. This model assumes an inverted neutrino

mass spectrum, with  $N_1$  being a light neutrino in the keV range (1-100 keV) acting as a dark matter candidate, and  $N_2$  and  $N_3$  being heavier (1-100 GeV). The small mass of  $N_1$  requires extremely small Yukawa couplings, leaving the lightest SM neutrino nearly massless. The heavier HNs generate SM neutrino masses via the Type-I seesaw mechanism and can even produce the baryon asymmetry of the universe via a process called leptogenesis [19], if their masses are close to each other. Moreover, they are in a mass range that is well suited for search in high-energy experiments.

### 3.3 Previous experimental searches

Current experimental searches for HNs span a wide range of masses and processes. I will give a short summary of the different searches and their resulting constraints on the heavy-light neutrino mixing, adapted from reference [22]. The heavy-light mixing elements  $U_{\ell N}$  represent the overlap between SM neutrino flavors and an additional HN state  $N$ :

$$\nu_\ell = \sum_{i=1}^3 U_{\ell i} \nu_i + U_{\ell N} N$$

where  $U_{\ell i}$  are the usual mixing elements of the standard PMNS matrix that relate the mass eigenstates of the SM neutrinos  $\nu_i$  with the flavor eigenstates  $\nu_\ell$ , and  $U_{\ell N}$  are the heavy-light mixing elements, which extend the PMNS matrix to incorporate the interaction between SM leptons and HNs.

Heavy neutrinos can be probed using different experimental techniques, each targeting specific production mechanisms and decay signatures. The search for low-mass HN candidates in the eV and keV range is performed using their production in beta decays. Electron neutrinos ( $\nu_e$ ) are typically produced in beta decays of unstable isotopes or during nuclear fission. If HNs mix with SM neutrinos, they can also be produced, provided that their mass is smaller than the maximum energy released during the process. The presence of HN then leads to measurable discontinuities in the energy spectrum of the emitted beta electrons. The size of each “kink” is proportional to  $|U_{eN}|^2$ , making it possible to measure or constrain the mixing element of the HN with the SM electron neutrino. Limits from these searches are shown in figure 3.1 in the eV to keV mass range.

Heavy neutrinos in the GeV and TeV range are probed in collider searches, as shown in figures 3.1, 3.2, and 3.3 from 2020. Heavy neutrinos can be produced through their mixing with SM neutrinos in processes involving W and Z bosons. Therefore, colliders focus on two main production mechanisms of HN: direct decay of on-shell W and Z boson, or weakly decaying mesons such as  $\pi$ , K, D, and B mesons.

Decays of W and Z bosons, which are abundantly produced in high-energy colliders, provide a key environment to search for HNs in the GeV and tens of GeV range. Key detector signatures for HNs are displaced vertices and lepton number violating processes. At the Large Electron-Positron (LEP) collider, HNs could be produced through on-shell Z, with  $e^+e^- \rightarrow Z \rightarrow N\nu_\ell$ . L3 and DELPHI searched for these decays with the HN decaying to  $N \rightarrow \ell^\mp W^\pm$ ,  $N \rightarrow \nu_\ell Z$  and  $N \rightarrow \nu_\ell H$ . The absence of signal resulted in a constraint of  $|U_{eN}|^2 < 10^{-4}$  in the range  $5 \text{ GeV} < m_N < 80 \text{ GeV}$  by L3 and  $|U_{eN}|^2 < 10^{-5}$  by DELPHI [23, 24, 25]. At the Large Hadron Collider (LHC), ATLAS, CMS, and LHCb have performed many HN searches in W decays [26, 27, 28, 29, 30, 31, 32, 33, 34], with limits on the coupling squared of HN to leptons ( $|U_{\ell N}|^2$ ) down to  $2 \times 10^{-7}$ . The production of HN is through  $W^\pm \rightarrow \ell^\pm N$ , following its decay to another lepton and an off-shell W boson which can itself decay to a lepton and a SM neutrino, two jets, or a charged pion.

While decays of  $W$  provide a good environment to search for HNs with mass of 5-50 GeV, the sensitivity decreases in lower HN masses as the small mass of HN compared to  $W$  makes it quite boosted in the lab frame and escape the detector before decaying. An alternative approach is to look for HN in weak decays of mesons such as  $\pi$ ,  $K$ ,  $D$ , and  $B$ . For instance,  $K^+ \rightarrow \ell^+ N$  constrains  $|U_{eN}|^2$  and  $|U_{\mu N}|^2$  for neutrinos with masses below the kaon mass. A set of experiments including TRIUMF PIENU [35], NA62 [36], Belle [37], NA3 [38], CHARM [39, 40] and PS191 [41] probe  $|U_{\ell N}|^2$  down to  $10^{-9}$  for  $m_N \sim 1$  GeV.

The best experimental environment to fill the gap between 1 and 5 GeV is the decays of the  $B$  meson, which are abundantly produced at the LHC. There are currently two such LHC searches available. One is a 2014 result from the LHCb experiment [42] which will be discussed in subsection 3.3.1 as the target experiment of my thesis project is also the LHCb experiment. Recently, the CMS experiment has also performed a search [43] in the mass range of 1 to 3 GeV using their 2018  $B$ -parking dataset, setting lower limits on  $|U_{\ell N}|^2$  down to  $2 \times 10^{-5}$ .

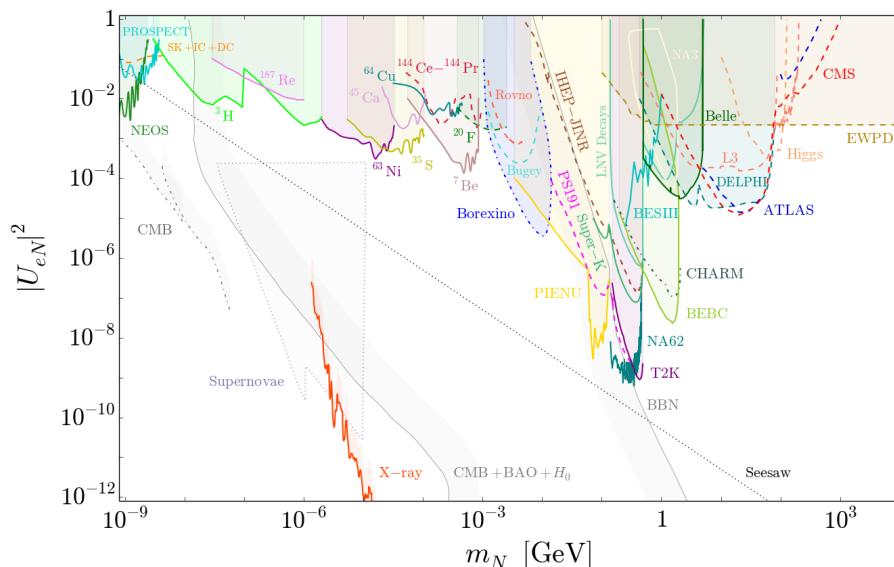


Figure 3.1: 2020 constraints on the mixing angle  $|U_{eN}|^2$  as a function of the HN mass  $m_N$ . The figure is taken from [22]

### 3.3.1 Search for heavy neutrinos at the LHCb experiment in $B^- \rightarrow \pi^+ \mu^- \mu^-$

The LHCb experiment conducted a search for HNs in the rare decay of  $B^- \rightarrow \pi^+ \mu^- \mu^-$ , as well as its charge conjugate [42]. This process is forbidden in the SM, but if Majorana neutrinos exist, they could mediate this process, violating lepton number conservation by producing two negatively charged muons in the final state. The Feynman diagram for this decay is shown in Figure 3.4.

This search used a dataset of proton-proton collisions at center-of-mass energies of 7 and 8 TeV with an integrated luminosity of  $3 \text{ fb}^{-1}$  collected by the LHCb detector. It targeted HNs with masses in the range of 250 to 5000 MeV and lifetimes of 0 to 1000 ps. They optimized their strategies for HNs with short lifetimes of 1 ps or less, dataset ( $\mathcal{S}$ ) (prompt), and for  $\tau_N$  up to 1000 ps, dataset ( $\mathcal{L}$ ) (displaced vertex). In both categories, only tracks starting in the VELO (vertex locator) were used. The main selection criteria were the selection of same-sign muons and the invariant mass of the  $\pi^+ \mu^- \mu^-$  system was required to match the  $B^-$  meson mass within detector resolution. The decay vertex of the  $B^-$  meson was reconstructed and events

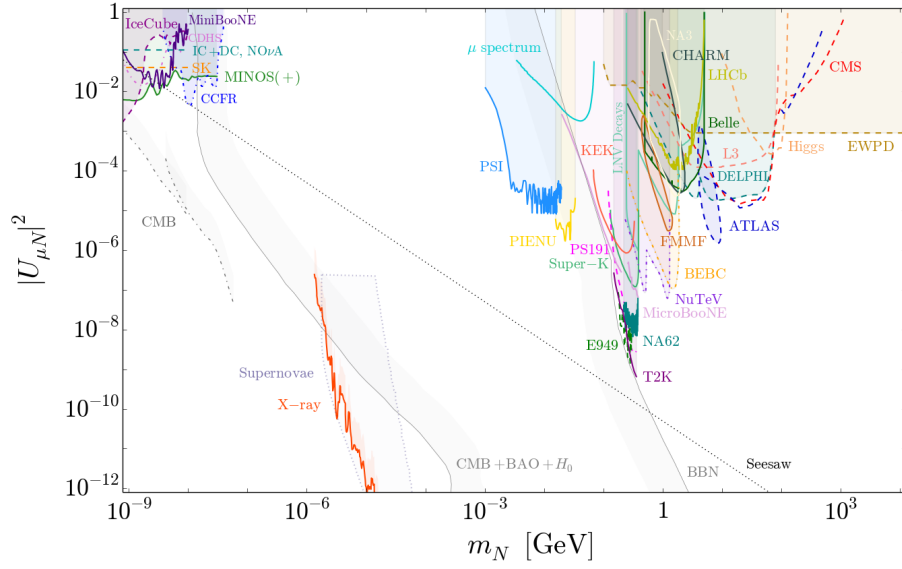


Figure 3.2: 2020 constraints on the mixing angle  $|U_{\mu N}|^2$  as a function of the HN mass  $m_N$ . The figure is taken from [22].

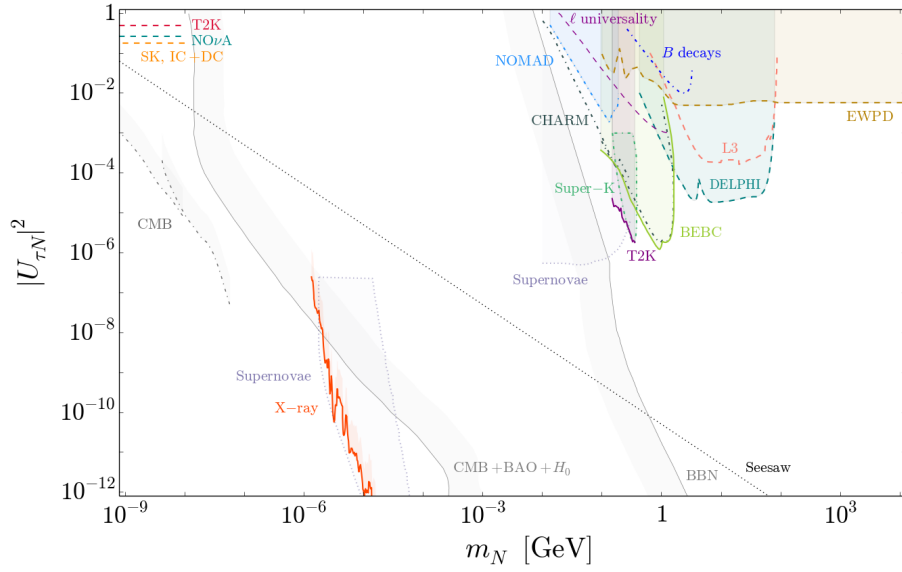


Figure 3.3: 2020 constraints on the mixing angle  $|U_{\tau N}|^2$  as a function of the HN mass  $m_N$ . The figure is taken from [22].

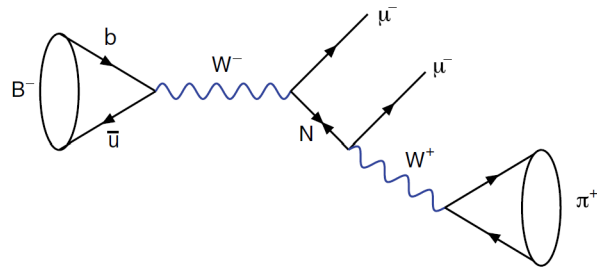


Figure 3.4: Feynman diagram for  $B^- \rightarrow \pi^+ \mu^- \mu^-$  with  $N$  denoting an on-shell heavy Majorana neutrino. Figure is taken from [42].

with vertices significantly displaced from the primary collision point were selected, consistent with the long lifetime of  $B^-$  mesons.

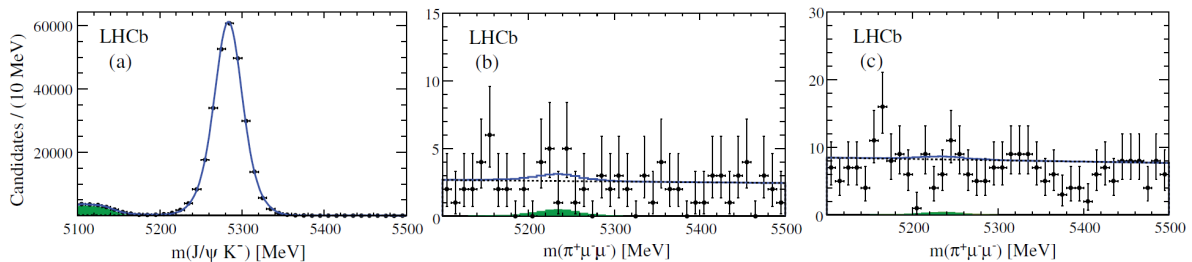


Figure 3.5: Invariant mass distributions with overlaid fits of candidate mass spectra for (a)  $J/\psi K^-$ , (b)  $\pi^+ \mu^- \mu^- \mathcal{L}$ , and (c)  $\pi^+ \mu^- \mu^- \mathcal{S}$ . Backgrounds are (green) shaded; they peak under the signal in (b) and (c). The dotted lines show the combinatorial backgrounds only. The solid line shows the sum of both backgrounds. Figure is taken from [42]

Two main backgrounds were considered in this analysis. The combinatorial background and the decay of  $B$  to charmonium, namely  $B \rightarrow J/\psi K^-$  and  $B \rightarrow \psi(2S)K^-$ , with further decay of the charmonium to two muons. The left plot of figure 3.5 shows the distribution of invariant mass of  $J/\psi K^-$  in a control region of opposite-sign muons. This is to extract a template shape for this background, which is then used in the signal region of the analysis, as shown in the other two plots for  $\mathcal{S}$  and  $\mathcal{L}$  strategies. It can be observed that the data-driven combinatorial background is the dominant background in this analysis, due to the efficient rejection of the charmonium background with opposite-sign muons. The branching ratio of  $B \rightarrow J/\psi K^-$  is the dominant source of systematic uncertainty (4.2%), followed by the modeling of the efficiency ratio (3.5%) and background modeling (3.5%), with a total systematic uncertainty of 6.6%.

No signal was observed in neither the  $\mathcal{S}$  nor  $\mathcal{L}$  samples. Hence, model-independent upper limits were placed on the product of branching ratios  $\text{BR}(B^- \rightarrow \mu^- N) \cdot \text{BR}(N \rightarrow \pi^+ \mu^-)$  as a function of the mass  $m_N$  and lifetime  $\tau_N$  or equivalently decay width  $\Gamma_N$ . For  $\mathcal{S}$  selected events, they find the upper limit for the branching ratio to be  $\text{BR}(B^- \rightarrow \pi^+ \mu^- \mu^-) < 4.0 \times 10^{-9}$  at 95% confidence level. For the  $\mathcal{L}$  sample, the detection efficiency also varies as a function of  $m_N$  and  $\tau_N$ . The detection efficiency peaks at a few picoseconds, then sharply declines until around 200 ps, after which it remains roughly constant up to about 1000 ps. Beyond this range, it gradually vanishes as most decays occur outside the vertex detector. The upper limits on the branching ratio for the  $\mathcal{L}$  sample are shown in figure 3.6.

These limits were translated into constraints on the mixing element  $|V_{\mu N}|^2$  between the muon and the HN with  $|V_{\mu N}|^2 \neq 0$  and  $|V_{iN}|^2 = 0$  for  $i \neq \mu$  using a theoretical model for the HN lifetime and its dependency on  $m_N$ .

$$\text{BR}(B^- \rightarrow \mu^- N) \cdot \text{BR}(N \rightarrow \pi^+ \mu^-) = \tau_B \tau_N \cdot \Gamma(B^- \rightarrow \mu^- N) \cdot \Gamma(N \rightarrow \pi^+ \mu^-),$$

where  $\tau_B$  and  $\tau_N$  are the lifetimes of  $B$  and  $N$ .  $\tau_N$  and both decay widths depend on  $m_N$  and  $|V_{\mu N}|^2$ . The decay widths were computed by Atre et al. in [44]. The total lifetime of the  $B$  is well known  $\tau_B = 1.671$  ps, whereas  $\tau_N$  was modeled in their paper [42]. The resulting 95% C.L. limit on  $|V_{\mu N}|^2$  is shown in figure 3.7 as a function of  $m_N$  for the original model derived in reference [42]. This model was later revised in reference [45], leading to more conservative constraints on the mixing elements and the limits on  $|V_{\mu N}|^2$ , also shown in figure 3.7.

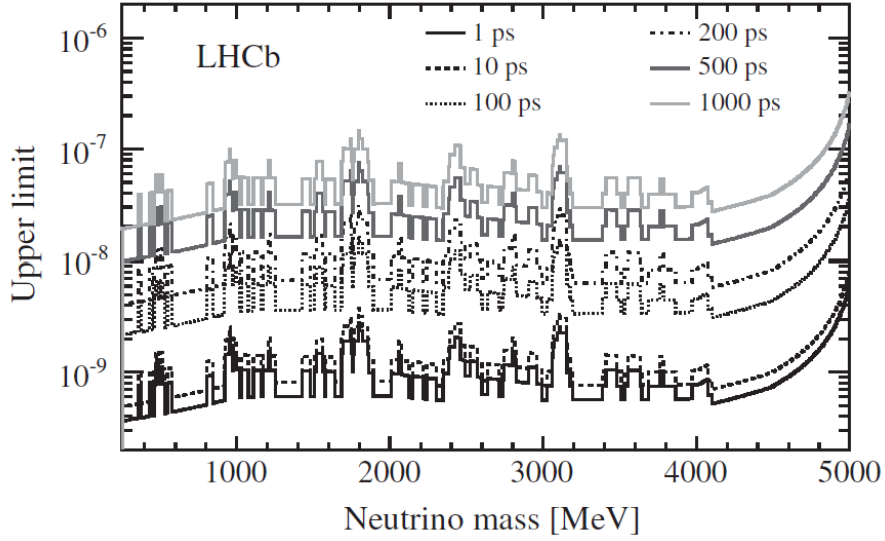


Figure 3.6: Upper limits on  $\text{BR}(B^- \rightarrow \pi^+ \mu^- \mu^-)$  at 95% C.L. as a function of  $m_N$ , in 5 MeV intervals, for specific values of  $\tau_N$ . Figure is taken from [42].

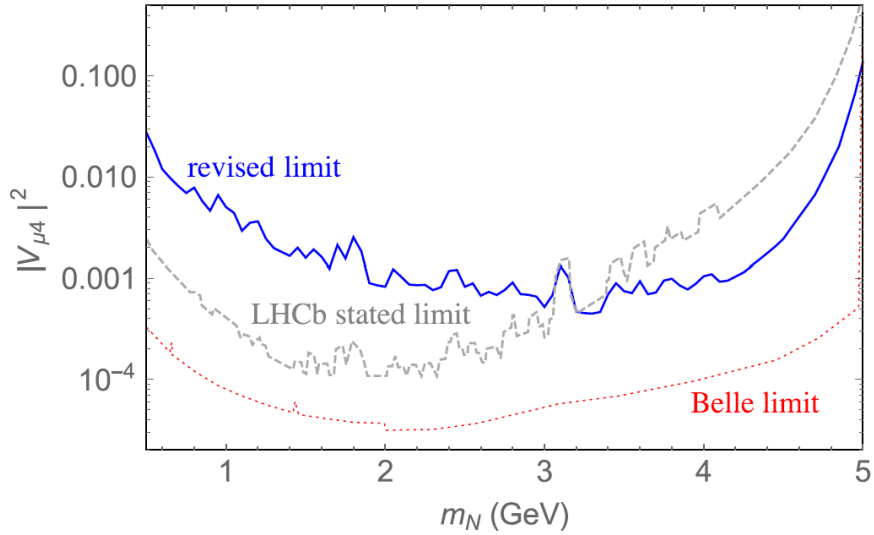


Figure 3.7: Upper limit on  $|V_{\mu N}|^2$  at 95% confidence level from the LHCb experiment. The dashed line shows the limit from [42]. The solid line shows the limit from the revised analysis [45]. For comparison, the lower dotted line shows the stated limit from Belle [37]. Figure is taken from [45].

### 3.4 Proposed search in $B_c$ decays

The paper ‘‘Unveiling the Heavy Neutrino Nature at LHCb’’ by Vasquez and Zamora-Saa [46] explores the possibility of detecting HNs introduced in  $\nu$ MSM in the decay of  $B_c$  mesons via the process  $B_c^+ \rightarrow \mu^+ N \rightarrow \mu^+ \mu^+ \tau^- \nu$  which involves an intermediate on-shell HN. This decay channel has a unique experimental signature, and my study aims to explore its detectability at LHCb in the GeV scale, which will be discussed in detail in chapter 5. This paper also suggests that a study of the kinematic properties of the final-state particles, such as the tau lepton energy spectrum, can help to reveal the Dirac or Majorana nature of the HN.  $B_c$  is preferred over  $B$  decays because the suppression due to CKM matrix elements is much stronger in  $B$  meson decays [47].

The Feynman diagrams for the studied processes are shown in figure 3.8. In this proposal, both lepton number violating (LNV) and lepton number conserving (LNC) processes are considered, as the HNs introduced in  $\nu$ MSM can also participate in LNV processes. While a Dirac HN can only mediate the LNC process, a Majorana HN can mediate both LNC and LNV processes, and therefore has both processes in its decay width. Hence, kinematically, the differential branching ratios vary between LNV and LNC channels and certain kinematic variables such as the energy of the final tau lepton and the angle  $\theta$  between the decay products could be used as potential indicators of whether the HN behaves as a Majorana or Dirac particle [48, 49].

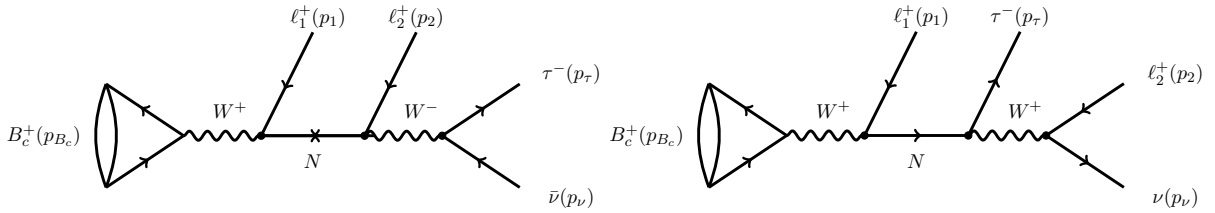


Figure 3.8: The feynman diagrams for the studied processes. Left: LNV process  $B_c^+ \rightarrow \ell_1^+ \ell_2^+ \tau^- \bar{\nu}$ . Right: LNC process  $B_c^+ \rightarrow \ell_1^+ \tau^- \ell_2^+ \nu$ . Where  $\ell$  is chosen to be  $\ell_1 = \ell_2 = \mu$  for their paper and my analysis. The figure is taken from reference [46].

The decay widths of the HN processes depend on the heavy-light mixing elements  $U_{\ell N}$ . In this proposal, they are set to  $|U_{eN}|^2 = 1 \times 10^{-8}$ ,  $|U_{\mu N}|^2 = 5 \times 10^{-7}$ , and  $|U_{\tau N}|^2 = 5 \times 10^{-6}$ , which are outside the excluded regions of the mixing elements [6, 50, 44, 22]. To account for experimental limitations, the branching ratios are modified by the acceptance factor due to the finite detector length and the detection efficiency factor  $\epsilon$ . The effective branching ratios were calculated numerically and are shown in figures 3.9 and 3.10, and table 3.1. The authors present the results for HN masses of  $m_N = 3.5, 4.0$  GeV, as the corresponding HN mixing parameters  $U_{\mu N}$  are subject to less experimental constraints [6, 50, 44, 22].

Figure 3.9 shows the dependence of differential branching ratios on the tau energy for HN masses  $m_N = 3.5, 4.0$  GeV and the differences in the shape of the distributions between a Majorana and Dirac HN. For instance, for HN mass of 4.0 GeV the Majorana BR dominates the Dirac BR in the tau energy range  $1.77 \leq E_\tau \leq 2.33$  GeV. In figure 3.10, the values of the effective branching ratios are shown for HN masses  $3 \lesssim m_N \lesssim 6$  GeV assuming a reconstruction efficiency of  $\epsilon = 0.8$  [51]. Given the higher mass of a tau lepton compared to a muon, in the HN rest frame, a bigger fraction of the HN energy is passed on to the tau, facilitating the distinguishing power between Dirac and Majorana scenarios shown in figure 3.9. This motivates the specific proposed decay channel involving a tau lepton compared to a muonic decay.

In table 3.1, the expected number of Majorana and Dirac HNs that can be produced at HL-LHC is shown, assuming a detector efficiency of 0.8 and a luminosity of  $\mathcal{L} = 10^{34} \text{ cm}^{-2} \text{ sec}^{-1}$  which corresponds to  $N_{B_c} \sim 5 \times 10^{10}$  number of  $B_c$  mesons produced per year [52].

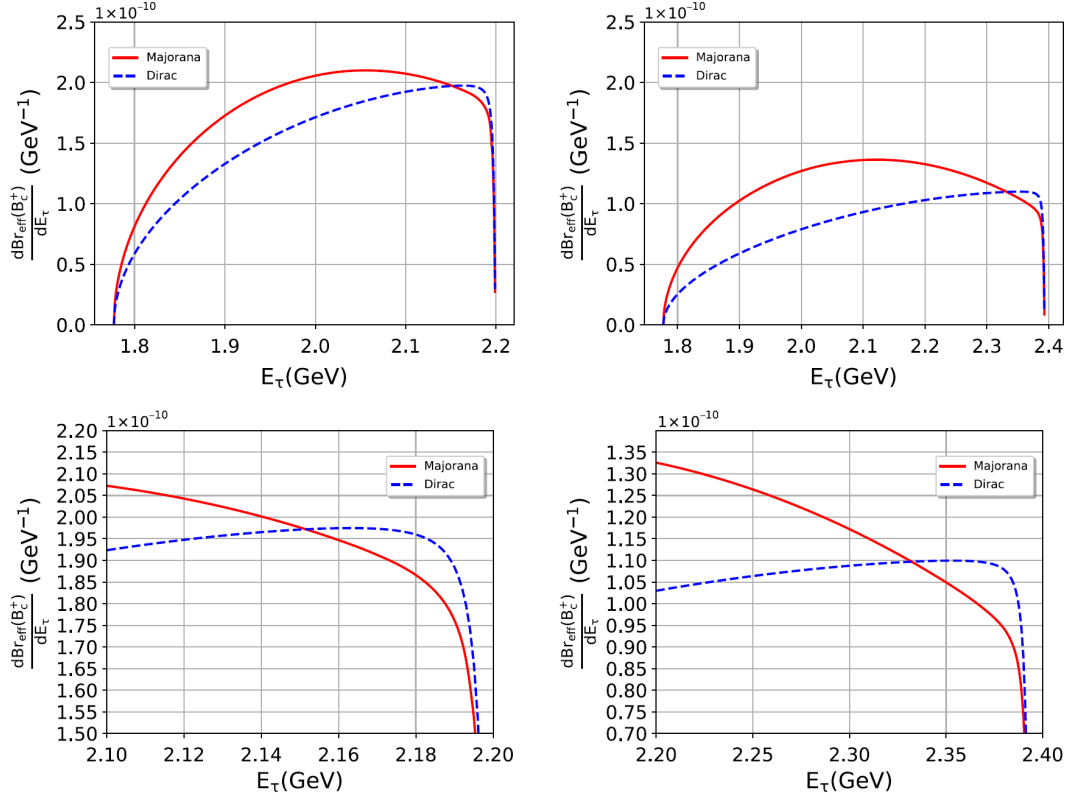


Figure 3.9: Distribution of Differential Branching ratio  $dBr/dE_\tau$  as a function of  $E_\tau$ . Top left:  $m_N = 3.5\text{GeV}$ , bottom left: zoomed in version of top left. Top right:  $m_N = 4.0\text{GeV}$ , bottom right: zoomed in version of top right. Here  $\epsilon = 1.0$ ,  $|U_{\mu N}|^2 = 5 \times 10^{-7}$ , and  $|U_{\tau N}|^2 = 5 \times 10^{-6}$ . The figure is taken from reference [46].

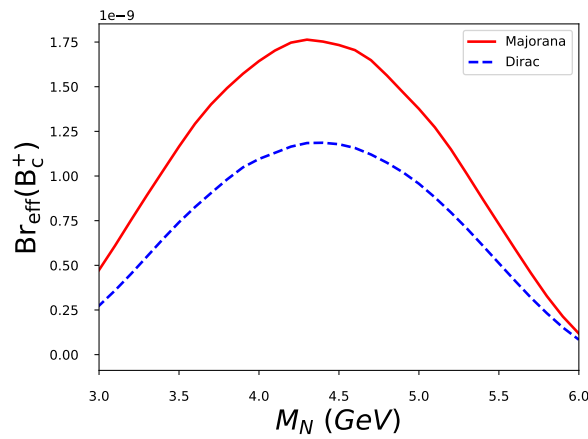


Figure 3.10: Effective branching ratios for a HN decaying through the process  $B_c^+ \rightarrow \mu^+ N \rightarrow \mu^+ \mu^+ \tau^- \nu$ . The red solid line shows the Majorana case and the dashed blue line the Dirac case. Here  $\epsilon = 0.8$ ,  $|U_{eN}|^2 = 5 \times 10^{-7}$  and  $|U_{\tau N}|^2 = 5 \times 10^{-6}$ . The figure is taken from reference [46].

$m_N(\text{GeV})$	Operation				
	time (years)	$Br^{\text{Dir}}$	$N_N^{\text{Dir}}$	$Br^{\text{Maj}}$	$N_N^{\text{Maj}}$
3.5	5	$1.34 \times 10^{-11}$	$\approx 3$	$2.47 \times 10^{-11}$	$\approx 6$
3.5	10	$1.34 \times 10^{-11}$	$\approx 7$	$2.47 \times 10^{-11}$	$\approx 12$
3.5	15	$1.34 \times 10^{-11}$	$\approx 11$	$2.47 \times 10^{-11}$	$\approx 19$
4.0	5	$2.55 \times 10^{-11}$	$\approx 6$	$4.27 \times 10^{-11}$	$\approx 11$
4.0	10	$2.55 \times 10^{-11}$	$\approx 13$	$4.27 \times 10^{-11}$	$\approx 21$
4.0	15	$2.55 \times 10^{-11}$	$\approx 19$	$4.27 \times 10^{-11}$	$\approx 32$

Table 3.1: Expected number of Dirac and Majorana heavy neutrinos observed by the LHCb experiment at HL-LHC, with an overall detector efficiency of 0.8 and squared couplings of  $|U_{\mu N}|^2 = 5 \times 10^{-7}$  and  $|U_{\tau N}|^2 = 5 \times 10^{-6}$ . The figure is taken from reference [46].

Therefore, according to this proposal, the data collected during the high-luminosity phase of LHCb might allow the identification of the HN. My study in chapter 5 aims to explore the detectability of these HNs in detail, including a simulation of the signal and background processes and obtaining realistic efficiency and acceptance factors for HNs in the mass ranges discussed. Not observing these HN processes in the LHCb experiment can lead to tighter exclusion limits on the mixing elements for a given HN mass.

# 4 The LHCb experiment

## 4.1 The Large Hadron Collider

The Large Hadron Collider (LHC) is the world’s largest and most powerful particle collider. With a circumference of 27 km, it is designed to accelerate beams of hadrons at very high energies in both directions and to collide them at four interaction points inside four large detectors; ATLAS, CMS, ALICE, and LHCb. Accelerated hadrons are primarily protons, but heavy ions such as lead or xenon are also used. The LHC tunnel is located about 100 meters under the ground near Geneva, Switzerland. As shown in figure 4.1, the LHC is part of CERN’s accelerator complex, in which protons are extracted from hydrogen, accelerated in multiple linear and circular accelerators, and eventually fed into the LHC, where they reach a collision energy of up to 13.6 TeV.

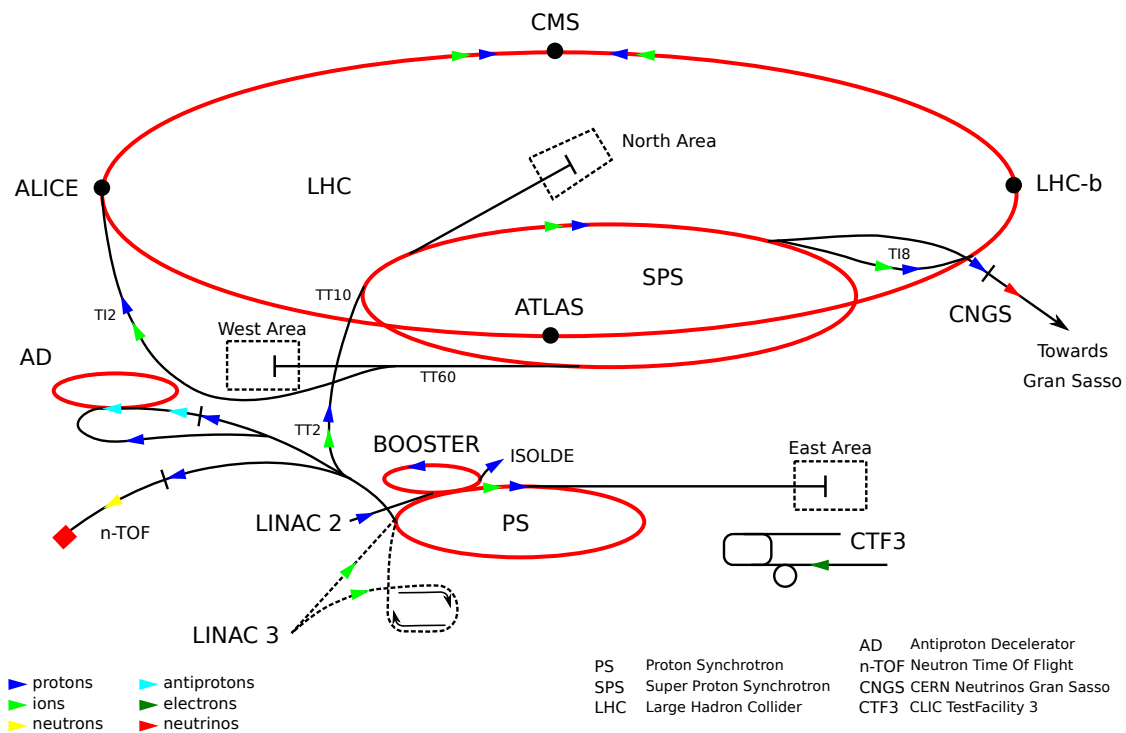


Figure 4.1: CERN’s accelerator complex. The figure is taken from reference [53].

The LHC accelerates the hadrons in two trains of bunches, one clockwise and one anticlockwise, and at each collision point the bunches are collided. The time distance between two consecutive bunches is 25 ns, corresponding to a collision rate of 40 MHz if all bunches collide. The effective collision rate is smaller at the LHCb collision point, with a visible collision rate of 30 MHz. Moreover, the average number of collisions from each bunch crossing, referred to as *pileup*, varies depending on the collision point. For instance, at the CMS and ATLAS collision points the pileup was around 35 in Run2 and 55 in Run3, while at the LHCb collision point the pileup was around 2 in Run2 and 6 in Run3.

The intensity of a collider is measured by its instantaneous luminosity  $\mathcal{L}$ , defined as the collision rate per second per beam area. While the LHC is the most intense collider ever built, the luminosity is lower at the LHCb interaction point compared to the CMS and ATLAS points, due to different physics goals.

Figure 4.2 shows the most updated schedule of the LHC. We are currently in the middle of Run 3 of the LHC, and after a long shutdown, the collision rate will significantly increase, marking the start of the High-Luminosity LHC (HL-LHC) era, from 2030 to 2041.

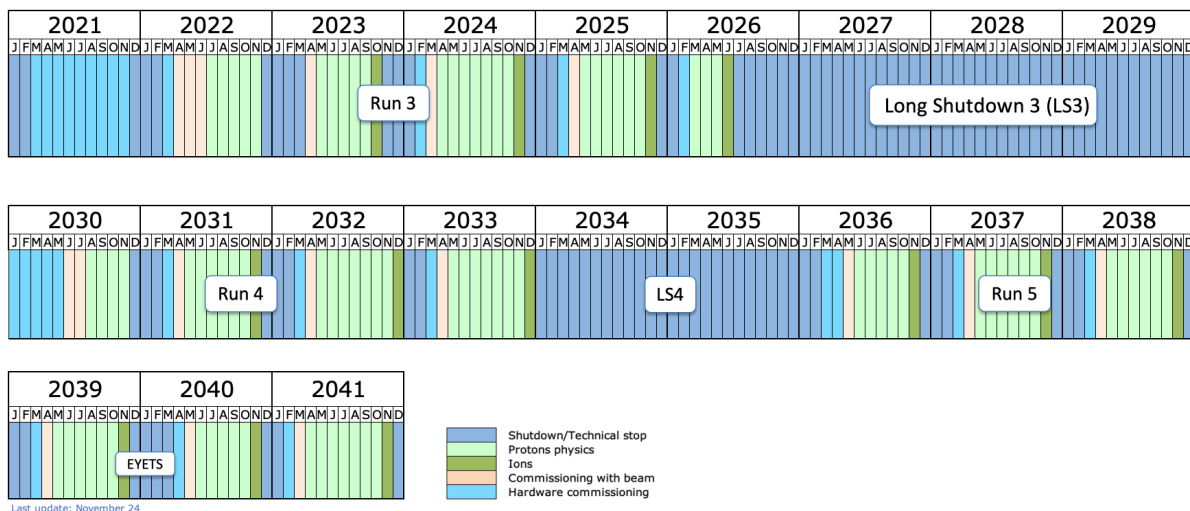


Figure 4.2: The updated schedule as of November 2024. HL-LHC operations are foreseen to start in 2030 and end in 2041. The figure is taken from reference [54].

## 4.2 The LHCb Experiment

The LHCb experiment [55] is one of the four experiments at the LHC. Its primary purpose is to search for new physics through studies of CP violation and decays of heavy-flavor hadrons, but it targets a wide range of physics program from electroweak to heavy ions and fixed target physics. Following a successful program in Run 1 and Run 2 of the LHC, with a total integrated luminosity of  $9 \text{ fb}^{-1}$ , the LHCb detector underwent a full upgrade during the LHC long shutdown 2, replacing almost all the subsystems and implementing a fully software-based online triggering system. In the following, the *upgrade 1* LHCb detector operating in Run 3 and Run 4 of the LHC will be discussed based on reference [56].

The LHCb detector, shown in figure 4.3, is a single-arm forward detector covering the pseudorapidity range  $2 < \eta < 5$ . The coordinate system used in this chapter and chapter 5 uses the nominal proton-proton interaction point as the origin, the direction of the beam towards the detector as  $+z$ , and the perpendicular plane as the *transverse plane*.

The LHCb detector comprises a set of subdetectors to identify outgoing particles from the interaction point and to measure their energy and momentum. The *tracking* system is responsible for finding the trajectory of charged particles before and after passing through the magnet shown in figure 4.3, in order to precisely measure their momentum vector. The most upstream tracking subsystem is the vertex locator (VELO), consisting of pixelated layers of silicon detectors, with the primary goal of precisely measuring the decay vertex positions and the displacement of the tracks from the primary vertex of the interaction. Due to the relatively high flight distance of beauty mesons, they can be identified by forming a secondary vertex far from the primary vertex

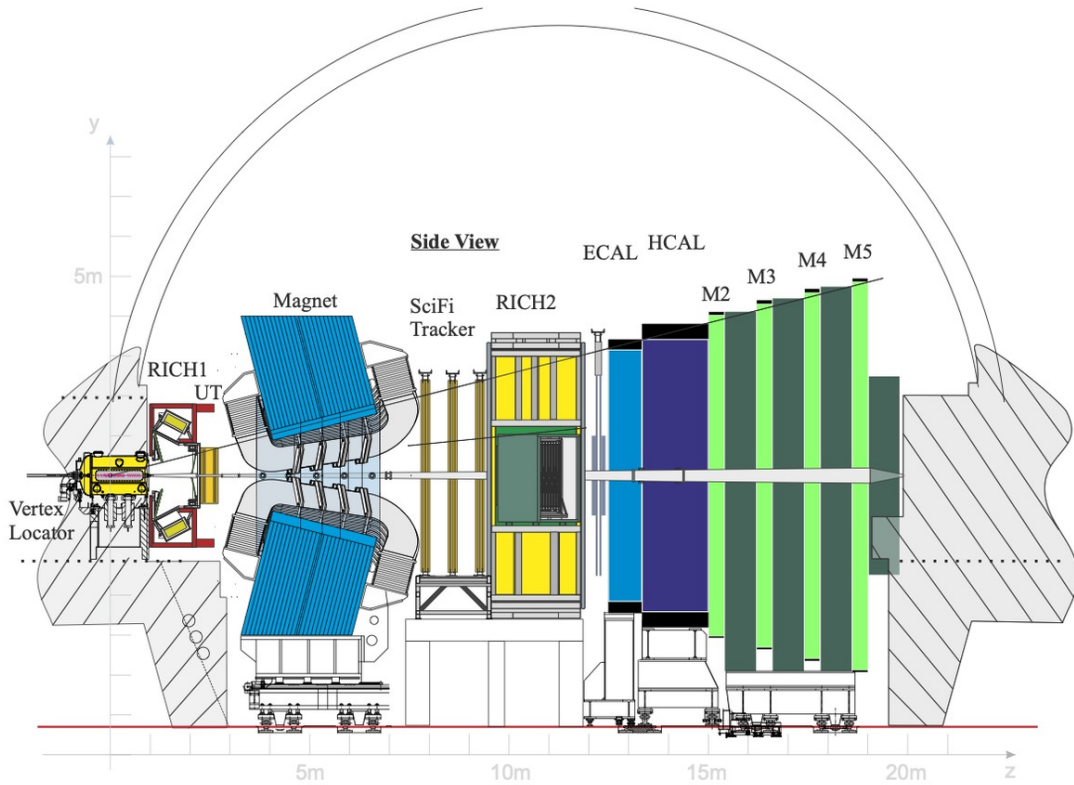


Figure 4.3: The LHCb detector. The figure is taken from reference [56].

of the interaction. Following VELO, the silicon-strip upstream tracker (UT) before the magnet and three stations of scintillating fiber tracker (SciFi) downstream of the magnet improve the tracking, and measure the momentum of charged particles based on their curvature in the magnetic field.

Two Ring Imaging CHerenkov detectors (RICH1 and RICH2) are responsible for particle identification. A sampling electromagnetic calorimeter (ECAL) is the subdetector responsible for measuring the energy of photons and electrons, while an iron-scintillator tile sampling hadronic calorimeter (HCAL) measures the energy of hadrons. The only SM particles expected to pass through the subsystems mentioned so far are muons and neutrinos. While the neutrinos are not visible to the LHCb detector, four stations of muon chambers interleaved with iron shielding measure the trajectory and therefore momentum of muons. This measurement is improved by matching the corresponding track with the one found in the tracking system.

One of the main upgrades of the LHCb detector was the exclusion of the simple inclusive selection criteria implemented in the hardware-based first trigger stage, based essentially on particle transverse momentum, as it would result in an effective loss of efficiency with increasing instantaneous luminosity, especially for the most abundant processes with hadrons in the final state and a low rejection rate of long-lived hadrons not containing heavy quarks [56]. The current triggering system reduces the data rate by a factor of 400 in a two-tier software-based system. The first stage of the triggering system is based primarily on the reconstruction of charged particles and reduces the data volume by roughly a factor of 20. The second stage performs the full reconstruction and selection of physics signatures.

# 5 Sensitivity of the LHCb experiment in heavy neutrino searches

## 5.1 Introduction

In chapter 3, I introduced heavy neutrinos (HN) from a theoretical point of view, the current status of searches for HN candidates, and finally, a proposal was presented in section 3.4 for a search for a HN using the LHCb experiment. The estimated efficiency and acceptance factors used in that proposal did not include the effects of detector geometry, background study, and signal reconstruction strategy.

In this chapter, I present a more detailed and realistic evaluation of the sensitivity of the LHCb experiment to HN searches. Various signal candidates and leading SM background processes mentioned in section 5.2 are simulated as described in section 5.3, including a precise geometrical acceptance of the LHCb detector and a corrected branching ratio for the specific reconstructible final state targeted in this analysis.

In section 5.4, kinematic distributions corresponding to the signal and background processes are presented. These distributions provide great insight on which regions of phase space are more desirable for signal selection, in order to for instance tune the online triggering strategy, as well as possible background rejection strategies. Moreover, given the detection of HN candidate events, the kinematic differences between the candidates used in this analysis provide sensitivity to understanding the characteristics of the HN, including its mass and whether it is a Majorana or Dirac particle.

Section 5.5 presents the estimated acceptance and efficiency factors from this analysis. These will be useful in obtaining a more realistic estimate of the effective number of expected events. Section 5.6 reviews the results of this analysis, including the effective branching ratio and the expected number of HN events in each year of HL-LHC, as a function of the HN coupling and mass.

## 5.2 Signal and background processes

The signal process in this analysis is  $B_c^+ \rightarrow \mu^+ \text{HN} \rightarrow \mu^+ \mu^+ \tau^- \bar{\nu}_\tau \rightarrow \mu^+ \mu^+ \mu^- \bar{\nu}_\mu \nu_\tau \bar{\nu}_\tau$ , shown in figure 5.1, as well as its charge conjugate. In addition, since the generator used in this analysis does not include the propagation of off-shell particles, here  $W^\pm$ , the Lepton Number Violating (LNV) process shown in figure 5.1 is kinematically equivalent to the Lepton Number Conserving (LNC) process shown on the right side of figure 3.8. In the kinematic comparisons in section 5.4, the *coupling squares* (mixing elements) are assumed to be at the upper limits used in the proposal paper [46], namely  $10^{-8}$  for electron,  $5 \times 10^{-7}$  for muon, and  $5 \times 10^{-6}$  for tau lepton. More precise limits as a function of mass were reported in subsection 3.3.

In this study, HN masses in the range of [1.9-6.0] GeV have been considered, while four mass points of 2.2, 3.0, 4.0, and 5.0 GeV are used in the kinematic plots of section 5.4. The proper flight distance ( $c\tau$ ) of the HN decreases with increasing coupling squares and in the simple case of HN coupling only to muons,  $c\tau$  times muon coupling square is constant for a given HN mass. The values used for coupling square times  $c\tau$  for mass points of 2.2, 3.0, 4.0, and 5.0 GeV are

4628.421, 879.474, 161.646, and 41.739 mm, respectively.

While the analysis of the signal and background kinematics and therefore signal acceptance and background rejection provides a more clear picture of the sensitivity, a priori we expect to be more sensitive to the HNs in the mass range of 4-5 GeV due to their higher branching ratio in the decays of  $B_c^+$  meson.

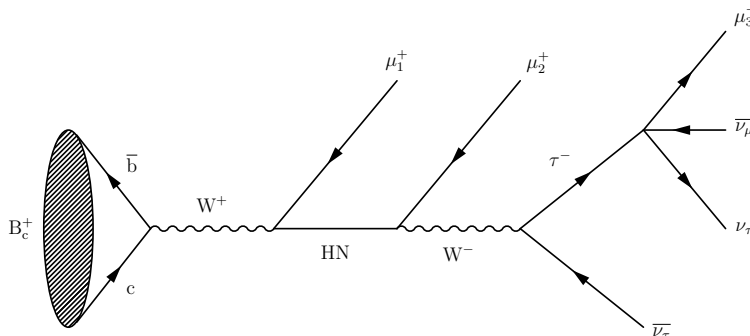


Figure 5.1: Feynman diagram of the signal process, demonstrating the decay of  $B_c^+$  to a heavy neutrino (HN), with three muons and three neutrinos in the final state.

I have considered three SM background processes, which are shown in figure 5.2. The first process, referred to hereafter as the  $D^*$  background, is the only process among the three for which the experimental cross section is available. It has a branching ratio of  $6.4 \times 10^{-4}$ , derived from available measurements for  $D^*$  production, conversion to  $D^0$ , and decay to the shown final states. The kaon can be falsely reconstructed as a muon with a small probability called *fake factor*, which is available [57] for the Run2 detector as a function of momentum. This momentum-dependent fake factor is applied to our simulation of the background process and is on average around 1%.

The second background process shown in figure 5.2 has the same final states as the signal, but it has never been observed, with an upper limit of  $1.6 \times 10^{-8}$  on its branching ratio. The third process involving a  $J/\psi$  has a branching ratio between the other two but is expected to be highly reducible using the clear  $J/\psi$  mass peak.

Overall, besides the combinatorial background which should be estimated with a full simulation or collision data and hence neglected in this analysis, these three background processes represent the three main categories of SM backgrounds for this analysis. It should be noted that in all SM background processes, the distance of closest approach of any dimuon pair is maximum a few hundreds of micrometers. Therefore, these processes are only relevant if the coupling of the HN is strong enough for it to fly less than half a millimeter. A more detailed discussion on background rejection will be given in section 5.5.

### 5.3 Monte Carlo simulation

As mentioned in section 5.1, the first step towards a more realistic sensitivity study is a Monte Carlo simulation of the signal and background processes, which provides a more realistic signal selection efficiency and acceptance. To do so, we use the RapidSim [58] generator. RapidSim

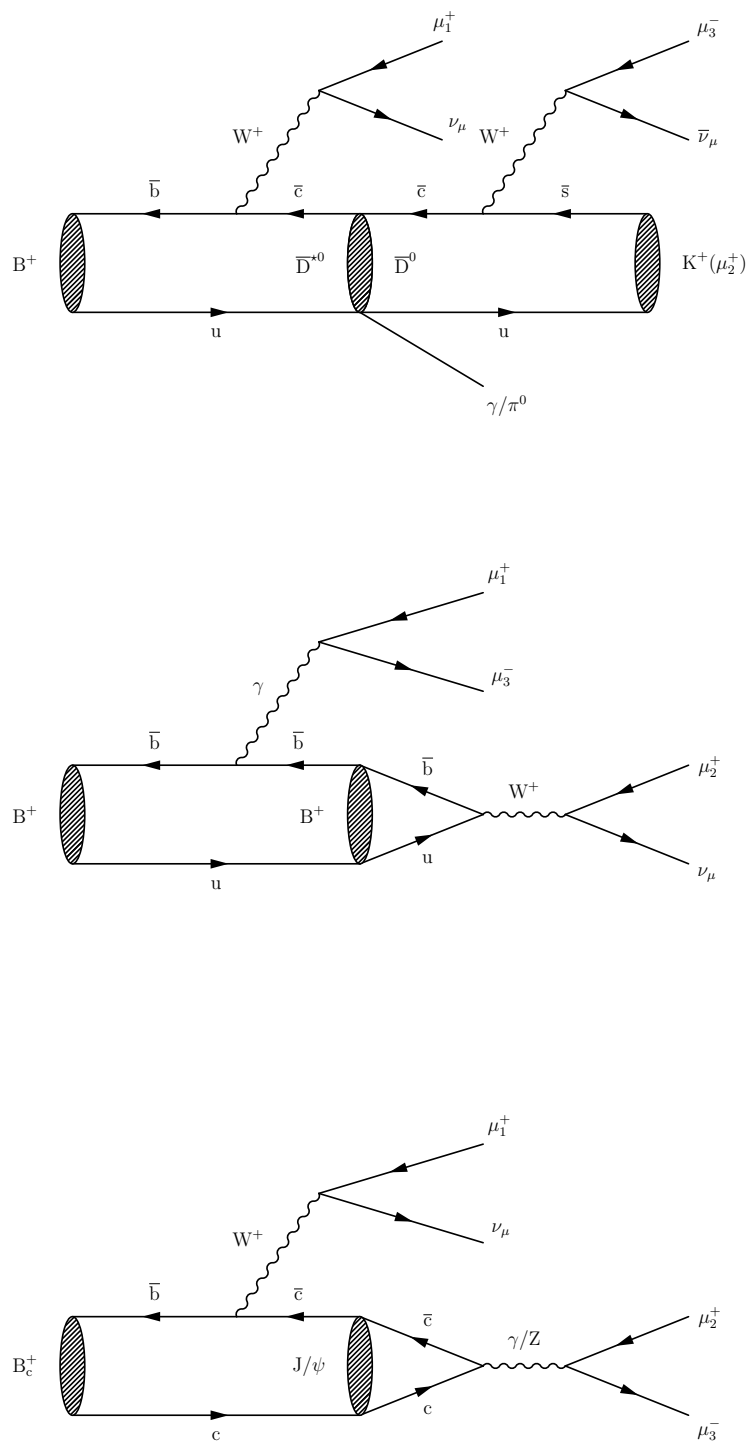


Figure 5.2: Feynman diagram of the three background processes in this analysis. In the top diagram, the kaon is expected to be falsely reconstructed as a muon.

is a lightweight generator for the fast simulation of phase-space decays of beauty and charm quark hadrons, allowing for quick studies of the properties of signal and background decays in particle-physics analyses, which perfectly matches with the goals of this sensitivity study.

The initial production of beauty and charm quarks is implemented using the fixed-to-next-to-the-leading order (FONLL) approximation model. The kinematics of the daughter particles can be smeared to account for detection resolution, and kinematic cuts can be applied to the daughter particles to account for the detector acceptance. In this study, all generated visible final-state particles are required to be within the acceptance phase space of the full LHCb detector, even in downstream and after the magnet kick, and their kinematics are smeared based on particle detection and identification at LHCb. Finally, RapidSim allows for the definition of new hypothetical particles with specific quantum numbers and decay rates. This feature was used in the simulation of the signal processes involving HN candidates.

Using RapidSim comes with two main disadvantages. Firstly, even though the kinematic smearing and identification efficiencies have been applied to the final states, precise detector effects can only be studied with a full material and readout simulation of the detector. For instance, effects such as false measurement of the charge of the tracks or flight distance resolutions are not included in the simulated samples. This is of course beyond the scope of this analysis but should be considered for a full analysis using the LHCb collision data. For this study, these effects have been added to the analysis of the simulated data whenever necessary, including the addition of flight distance smearing.

The second and more relevant disadvantage of RapidSim is the lack of off-shell propagators. For instance, in the signal process shown in figure 5.1, both  $\mu_2^+$  and  $\tau^-$  are direct daughters of the HN in RapidSim. This will make it impossible to kinematically distinguish the LNV and LNC signal processes, which has been shown to be quite useful in determining the Majorana or Dirac nature of the HN.

## 5.4 Kinematics of signal and background processes

Following a Monte Carlo simulation of the signal and background candidates, the next step towards estimating the sensitivity of LHCb to search for a HN candidate is to search for kinematic selections that veto background events as much as possible, while maintaining a high signal efficiency to achieve a high signal significance.

Kinematic signal selections can in principle be different for various signal candidates, given that variations in the HN mass affect the kinematics of the signal. However, to ensure simplicity and practicality, selections that are common for all signal candidates are favorable.

In this section, signal candidates with HN masses of 2.2, 3.0, 4.0, and 5.0 GeV are compared with three background processes shown in figure 5.2. For visible final state objects and their reconstructed mother particles, the comparison is made in kinematic variables such as transverse momentum ( $p_T$ ), energy, flight distance, and angular distributions. All kinematic distributions in this analysis have been normalized to have an integral of 1, to emphasize the shape variations. More details on absolute acceptance and efficiency will be discussed in section 5.5.

A few selections are already applied on the following kinematic distributions in this section. All three final-state muons are required to be within the LHCb acceptance region, including the downstream region after the magnet kick. Moreover, in this study we have required all three muons to have a  $p_T$  above 1.3 GeV, resembling a possible trigger threshold. While such a trigger threshold is useful in the study of kinematics and the effect of trigger on signal acceptance, when discussing the best estimates for the signal acceptance and estimated number of HN candidates in section 5.5, we assume that an online triggering system requiring only the two same-sign muons without any online threshold can also be studied and developed for this analysis, if not

already present.

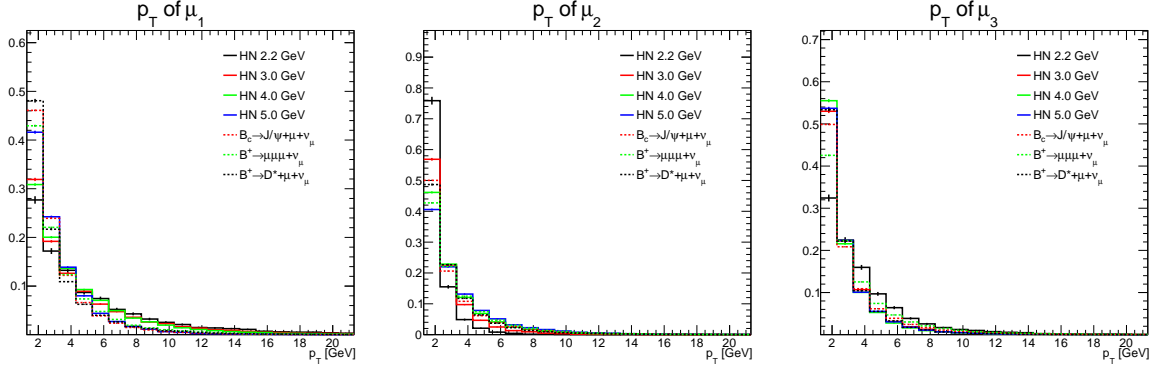


Figure 5.3: Distributions of  $p_T$  of three final state muons. Four signal candidates with heavy neutrino masses of 2.2, 3.0, 4.0, and 5.0 GeV are shown with solid lines, while three background processes are shown with dashed lines.

Figure 5.3 shows the HN muon  $p_T$  distributions for the three final-state muons shown in the signal schematic in figure 5.1. The higher the mass of HN, a lower fraction of the initial B energy will be transferred to  $\mu_1^+$  transverse momentum, hence the softer  $p_T$  distribution of  $\mu_1^+$  for HN with mass 5 GeV than 2.2 GeV. The  $p_T$  distribution of  $\mu_2^+$  gets harder for higher masses, so a large fraction of the simulated events for HN mass of 2.2 GeV do not pass the 1.3 GeV trigger threshold on  $\mu_2^+$ . This is mainly due to the fact that the tau lepton mass (1.777 GeV) is too close to the HN mass and much higher than the muon mass, so the tau lepton takes a large fraction of the HN energy.

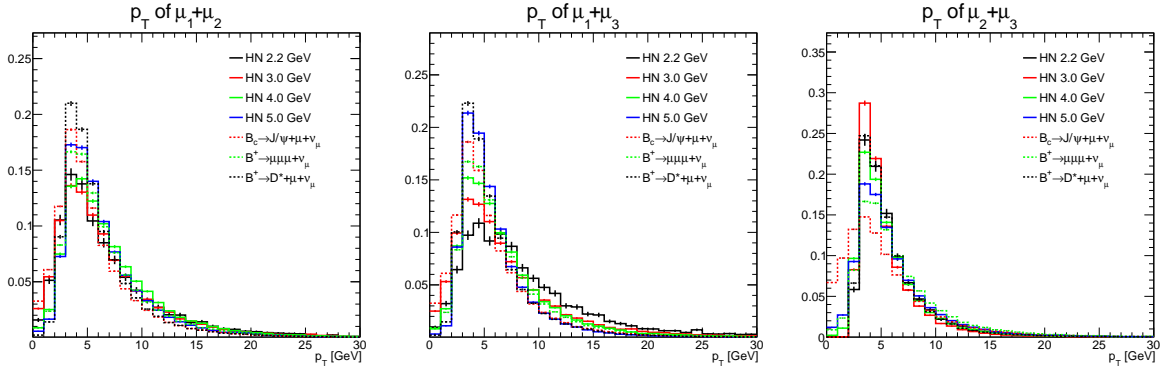


Figure 5.4: Distributions of vector sum  $p_T$  of each muon pair. The right plot represents the visible  $p_T$  of the heavy neutrino. Four signal candidates with heavy neutrino masses of 2.2, 3.0, 4.0, and 5.0 GeV are shown with solid lines, while three background processes are shown with dashed lines.

Figure 5.4 shows normalized distributions of the vector sum  $p_T$  of each pair of muons. The left plot shows some potential to distinguish and reduce the  $D^*$  background with the highest branching ratio. The middle plot shows that for searches targeted to lower-mass HN candidates, sensitivity increases in higher  $p_T$  ranges. This can be helpful as we will see later that these low-mass candidates are expected to have a small branching ratio in  $B_c$  decays. The right plot represents the visible  $p_T$  of the HN, but no clear shape difference is observed either between the signal candidates or when compared to the background distributions. This can be compared with the left plot of figure 5.5, where the true  $p_T$  of the HN is shown. The increase in  $p_T$

when the HN mass decreases is more clear in the *true*  $p_T$  distribution, including all non-visible daughters. The right plot of figure 5.5 shows the true  $p_T$  distributions of the  $B_c^+$ . The difference in the  $p_T$  shapes comes from the fact that for lower mass HNs, the initial energy of the  $B_c^+$  has to be higher for the event to pass the acceptance and trigger selections. This will be further clarified when reviewing the acceptance and efficiencies in section 5.5.

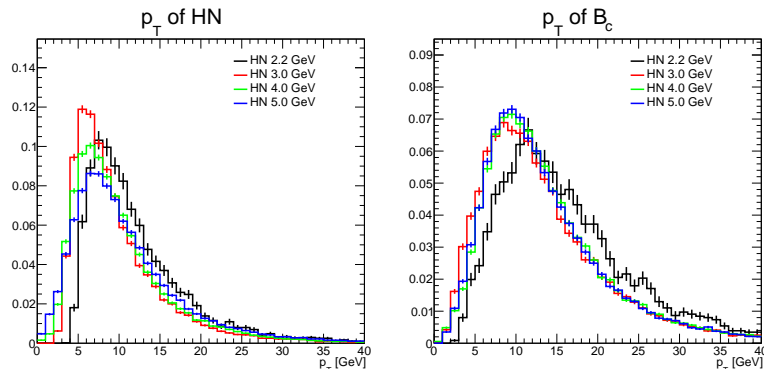


Figure 5.5: Distributions of true  $p_T$  of the heavy neutrino (left), and true  $p_T$  of  $B_c^+$  (right). Four signal candidates with heavy neutrino masses of 2.2, 3.0, 4.0, and 5.0 GeV are shown with solid lines, while three background processes are shown with dashed lines.

The distributions of the energy of the three final-state muons are shown in figure 5.6. It can be observed that using  $\mu_1^+$  and to some extent  $\mu_3^-$  energies, one can reduce the  $D^*$  background. Once again, the  $\mu_2^+$  energy distribution emphasizes the need to go as low as possible in energy or momentum thresholds to reconstruct the low-mass HN candidates.

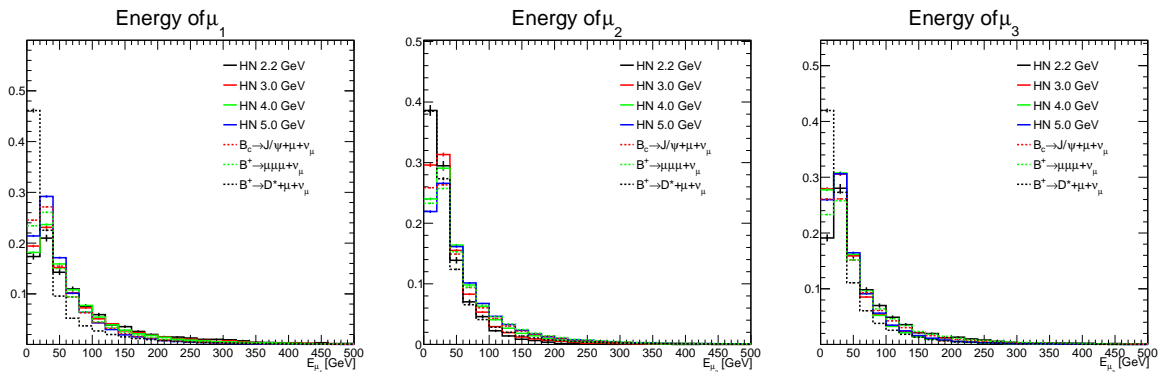


Figure 5.6: Distributions of energy of three final state muons. Four signal candidates with heavy neutrino masses of 2.2, 3.0, 4.0, and 5.0 GeV are shown with solid lines, while three background processes are shown with dashed lines.

As shown in figure 3.9, due to the different kinematics of the LNC and LNV signal processes, the energy of the tau in the HN rest frame can reveal the Majorana or Dirac nature of the HN. However, unfortunately the RapidSim generator does not facilitate a straightforward addition of off-shell particles like the W bosons in figure 5.1, meaning that  $\mu_2^+$  and tau are both connected to the HN decay vertex and we cannot distinguish between LNV and LNC processes. Nevertheless, the energy of tau in the HN rest frame for true HN and tau particles is shown in the left plot of figure 5.7. We can see that our distributions resemble the Dirac HN distribution more, which is only present in the LNC process.

The observable distributions from a real detector can only use the visible final states. The

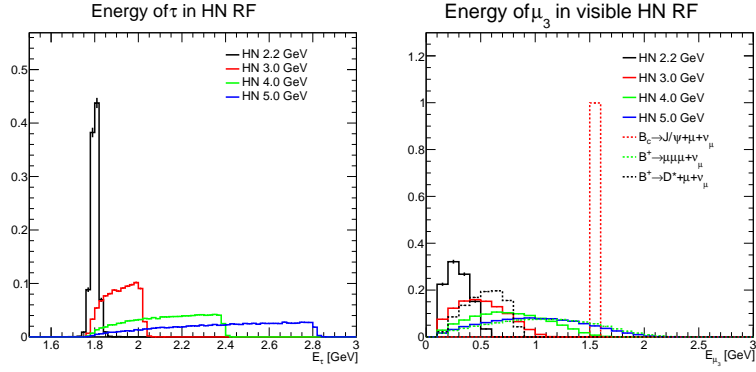


Figure 5.7: Distribution of energy of tau in the heavy neutrino rest frame. Four signal candidates with heavy neutrino masses of 2.2, 3.0, 4.0, and 5.0 GeV are shown with solid lines, while three background processes are shown with dashed lines. The left plot uses the true heavy neutrino and tau, while the right plot uses only their visible decay products.

right plot of figure 5.7 shows the energy of  $\mu_3^-$ , as the visible part of the tau, in the rest frame of the vector sum of  $\mu_2^+$  and  $\mu_3^-$ , as the visible part of the HN. Firstly, it can already be seen that this distribution has a good potential for reducing the  $J/\psi$  and  $D^*$  backgrounds. Secondly, even though the visible distributions differ from the true ones, such distributions could be different between the LNV and LNC processes, and with a more advanced generator we can realize the sensitivity of this analysis for not only a potential observation, but hints on the Dirac or Majorana nature of the HN.

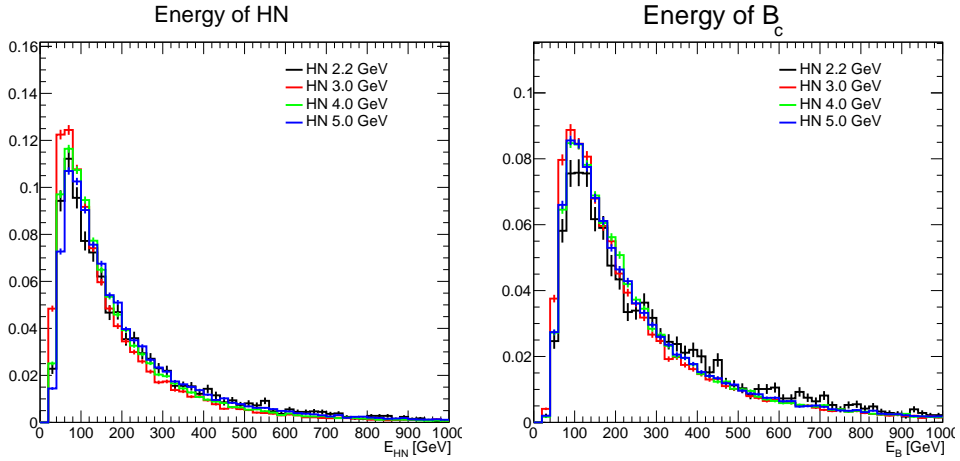


Figure 5.8: Distributions of true energy of the heavy neutrino (left) and  $B_c^+$  (right). Four signal candidates with heavy neutrino masses of 2.2, 3.0, 4.0, and 5.0 GeV are shown with solid lines, while three background processes are shown with dashed lines.

Figure 5.8 shows the distributions of the energy of the HN and  $B_c^+$  for all signal candidates, which unfortunately does not provide any discrimination power even for the true energy values.

Figure 5.9 shows the difference in azimuthal angle ( $\Delta\phi$ ) between each pair of muons. While these distributions are correlated with the dimuon  $p_T$  distributions shown in figure 5.4, one can observe that the  $\Delta\phi$  distributions provide much stronger discrimination power both between the signal candidates and when compared to the background distributions. The  $\Delta\phi$  shows to

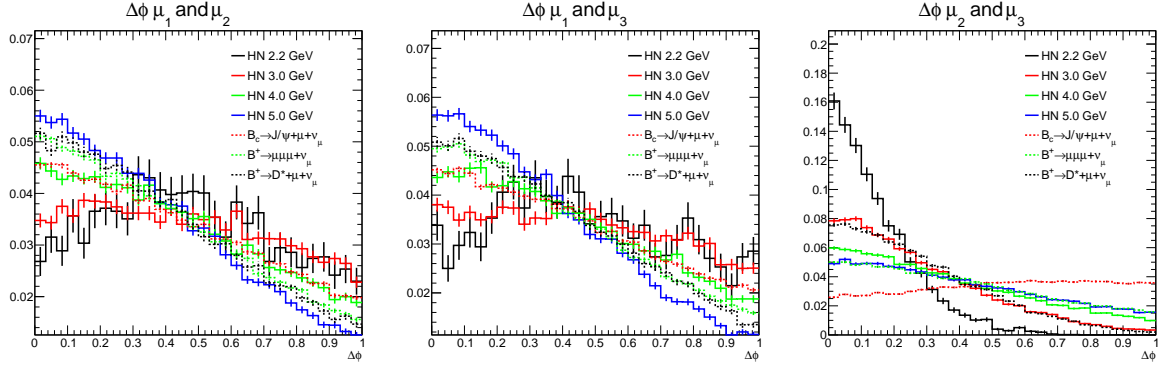


Figure 5.9: Distributions of difference in azimuthal angle,  $\Delta\phi$ , between each muon pair. Four signal candidates with heavy neutrino masses of 2.2, 3.0, 4.0, and 5.0 GeV are shown with solid lines, while three background processes are shown with dashed lines.

decrease with increasing HN mass for the left and middle plot, and vice versa for the right plot. The  $\Delta\phi$  between the two muons from  $J/\psi$  seem to be evenly distributed as shown in the right plot.

Figure 5.10 shows the distributions of the Lorentz-invariant opening angle ( $\Delta R$ ) between each pair of muons, defined as the quadrature sum of the difference in azimuthal angle and in pseudorapidity. It can be seen that the discrimination power of  $\Delta R$  distributions is lower than the corresponding  $\Delta\phi$  distributions.

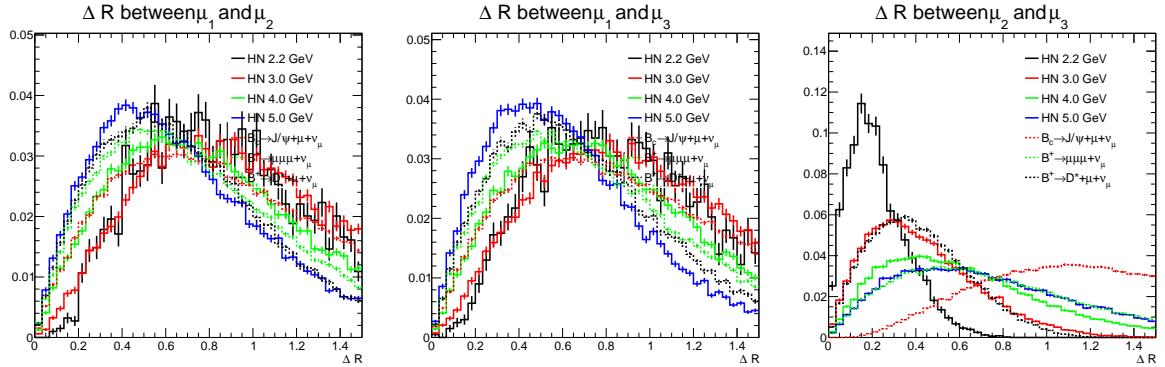


Figure 5.10: Distributions of  $\Delta R$  between each muon pair. Four signal candidates with heavy neutrino masses of 2.2, 3.0, 4.0, and 5.0 GeV are shown with solid lines, while three background processes are shown with dashed lines.

Figure 5.11 shows the invariant mass distributions of each muon pair. In terms of distinguishing between the HN candidates, the invariant mass distributions show the sensitivity to identify the mass of the potentially observed HN candidate. More importantly, the main discrimination power comes from the right plot for the invariant mass of  $\mu_2^+$  and  $\mu_3^-$ . For the  $J/\psi$  background, this variable shows the  $J/\psi$  invariant mass which is a clear and narrow peak around 3.1 GeV. Moreover, in the  $D^*$  background with significantly higher branching ratio, the  $D^0$  with a mass of 1.865 GeV decays to  $\mu_3^-$ , a neutrino, and a kaon which is reconstructed as  $\mu_2^+$ . Therefore, the invariant mass of  $\mu_2^+$  and  $\mu_3^-$  should be lower than the  $D^0$  mass, giving a high sensitivity to searches for higher mass HNs above 4 GeV.

The left plot of figure 5.12 shows the true invariant mass of the HN candidates, reconstructed from all 4-vectors of their decay candidates including the neutrinos. Apart from the natural

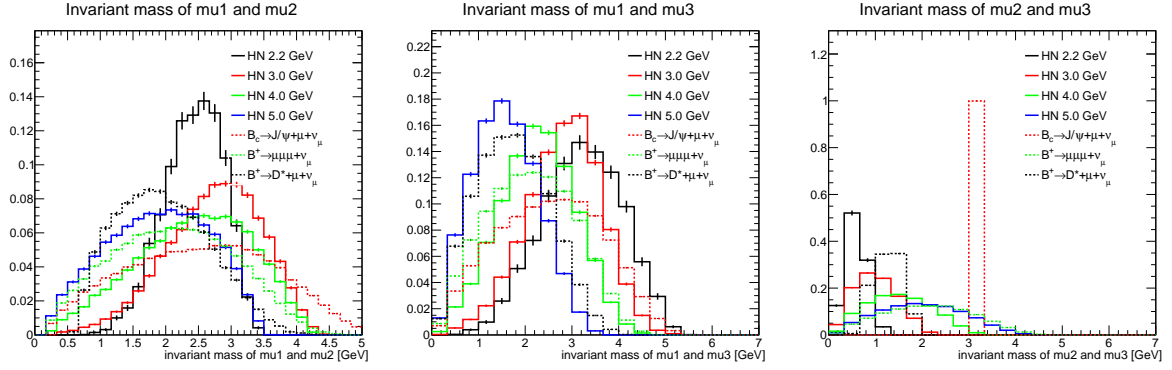


Figure 5.11: Distributions of invariant mass of each muon pair. Four signal candidates with heavy neutrino masses of 2.2, 3.0, 4.0, and 5.0 GeV are shown with solid lines, while three background processes are shown with dashed lines.

decay width and the smearing of visible final states, all candidates show a very narrow mass peak. This is not the case when reconstructing the visible mass of the HN, which is the invariant mass of  $\mu_2^+$  and  $\mu_3^-$ . As mentioned when discussing figure 5.11, this variable has a great potential for discriminating between the signal candidates and vetoing the main background processes. The right plot of figure 5.12 shows the visible invariant mass of the  $B_c^+$  candidate, namely all three final-state muons. It shows a potential for further reducing the  $J/\psi$  background, but naturally not as clean as the middle plot.

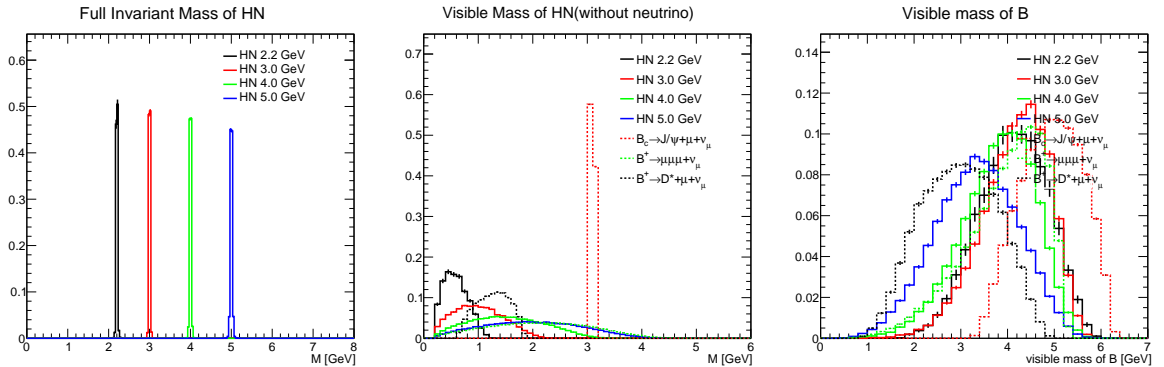


Figure 5.12: Distributions of true invariant mass of heavy neutrinos (left), visible mass of heavy neutrinos (middle), and visible mass of the B meson (right). Four signal candidates with heavy neutrino masses of 2.2, 3.0, 4.0, and 5.0 GeV are shown with solid lines, while three background processes are shown with dashed lines.

Given the low coupling of the HN with SM particles, it is expected to fly longer than most SM particles before decaying. Theoretically, the proper flight distance, defined as  $c\tau$ , with  $c$  the speed of light and  $\tau$  the proper decay time, can be derived from the decay width of the HN. As input for this analysis, we have theoretically determined the  $c\tau$  as a function of the mass and the coupling square ( $\alpha_\ell^2$ , or  $|U_{\ell N}|^2$  with the notation of chapter 3) of the HN to each lepton ( $\ell$ ). For kinematic comparisons in the following plots, the  $\alpha_\ell^2$  are assumed to be at the upper limits used in the proposal paper [46], namely  $10^{-8}$  for  $\ell = \text{electron}$ ,  $5 \times 10^{-7}$  for  $\ell = \text{muon}$ , and  $5 \times 10^{-6}$  for  $\ell = \text{tau lepton}$ . The resulting  $c\tau$  as a function of mass is then given as an input to RapidSim to simulate the corresponding exponential flight distances. The  $c\tau$  values used for 2.2, 3.0, 4.0, and 5.0 GeV HN candidates are 4628.421, 879.474, 161.646, and 41.739 mm, respectively.

Following the simulation, I measure the flight distance per event by calculating the distance between the production and decay vertices of the HN in x, y, and z directions. Figure 5.13 shows the distribution of the flight distance of the HN, shown separately when projected along the beam (z axis) and the transverse plane. It can be seen that the HN flies less with increasing mass, as expected from the  $c\tau$  values, and for each mass point it flies less in the transverse plane than along the z axis, due to the forward nature of these events.

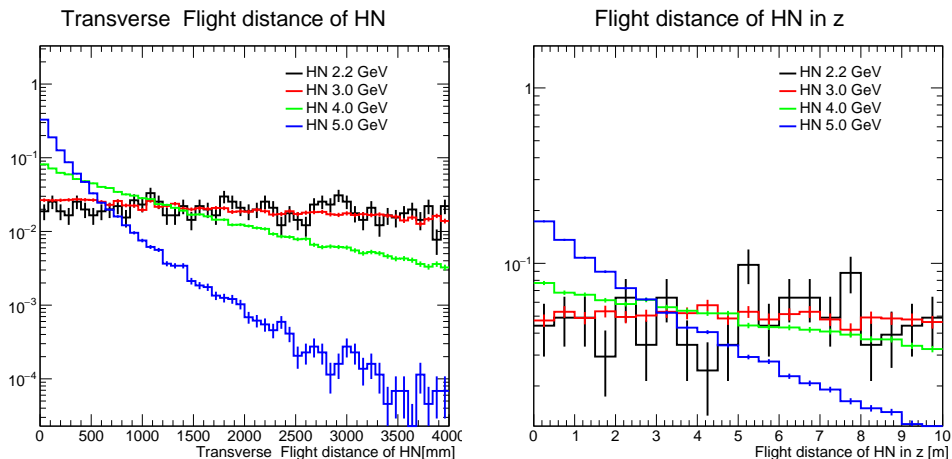


Figure 5.13: Distributions of the flight distance of the heavy neutrinos in the transverse plane (left) and along the beam (right). Four signal candidates with heavy neutrino masses of 2.2, 3.0, 4.0, and 5.0 GeV are shown with solid lines.

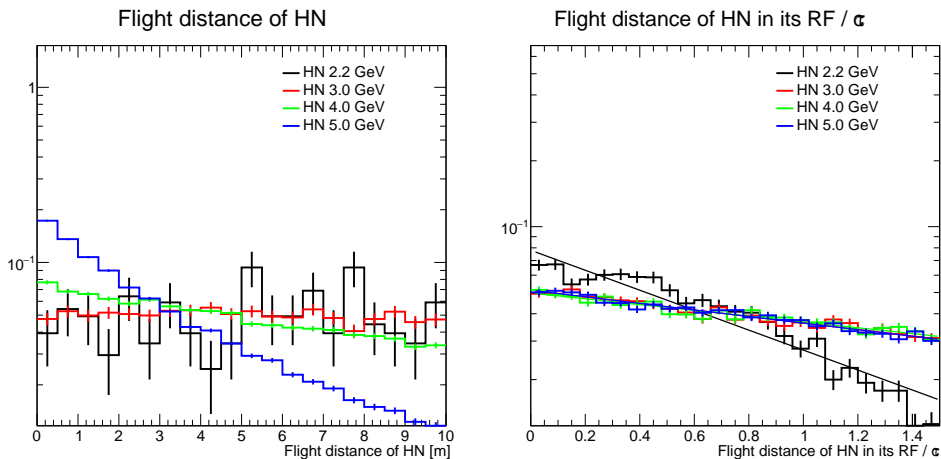


Figure 5.14: Distributions of the total flight distance of the heavy neutrinos in the lab frame (left) and in the heavy neutrino rest frame (right). Four signal candidates with heavy neutrino masses of 2.2, 3.0, 4.0, and 5.0 GeV are shown with solid lines.

The left plot in figure 5.14 shows the total flight distance in the lab frame, given by the quadratic sum of the x, y, and z components. It can be seen that the distributions do not precisely match with an exponential Poisson decay, which is due to the fact that HNs are boosted in the lab frame with energies varying from event to event. If we boost back the flight distance to the HN rest frame for each event, we can expect an exponential distribution, the slope of which determines the  $c\tau$ . This is shown in the right plot of figure 5.14, where I plot the flight distance in the HN rest frame, divided by the theoretical  $c\tau$ . The division by  $c\tau$  is for a

visualization purpose, to obtain similar distributions regardless of the mass. The fact that these distributions are firstly exponential, and secondly similar for all masses apart from statistical fluctuations, validates both the flight distance simulation and the measurement method.

## 5.5 Acceptance and efficiency

In this section, I present different factors that contribute to the acceptance and efficiency of recording HN events. This includes geometric acceptance of the LHCb detector, efficiency of triggering the final-state muons, and efficiency of signal selection criteria.

### 5.5.1 Trigger and geometrical acceptance

In terms of trigger efficiency, one of the main contributing factors is the trigger threshold on the muon  $p_T$ . Figure 5.15 shows the trigger efficiency as a function of this online trigger threshold on muon  $p_T$ , assuming that all three muons must pass this threshold. It can be seen that such  $p_T$  thresholds affect the lower-mass HN candidates more, which already have a lower branching ratio, as will be seen later. However, in a realistic trigger path, not all three muons have to pass the trigger threshold, and certainly not the same threshold as requiring a single muon in the event.

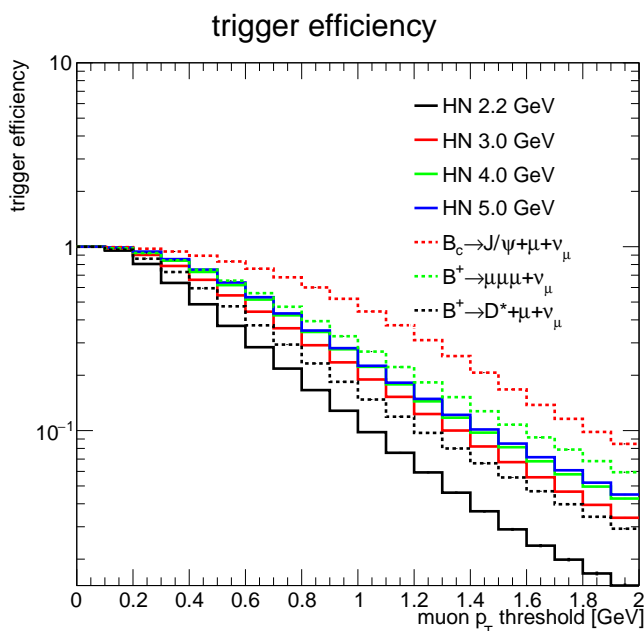


Figure 5.15: Efficiency of recording an event with all three muons within the acceptance region of the LHCb and having a  $p_T$  above an online trigger threshold, as a function of this threshold.

The geometrical acceptance of the LHCb detector for HN signal events is also one of the deliverables of my analysis, given that in the theoretical predictions [46] for the sensitivity to HNs, a complete  $4\pi$  acceptance was assumed, which needed to be corrected using RapidSim. In this analysis, we require all three final-state muons to be within the geometrical acceptance region of the LHCb detector, even downstream after the magnet kick. The effect of such a requirement is seen in figure 5.16, which shows the sequential effect on acceptance times efficiency after

applying a requirement on top of the previous ones. It can be observed that the low-mass HN suffers more from the geometrical requirement.

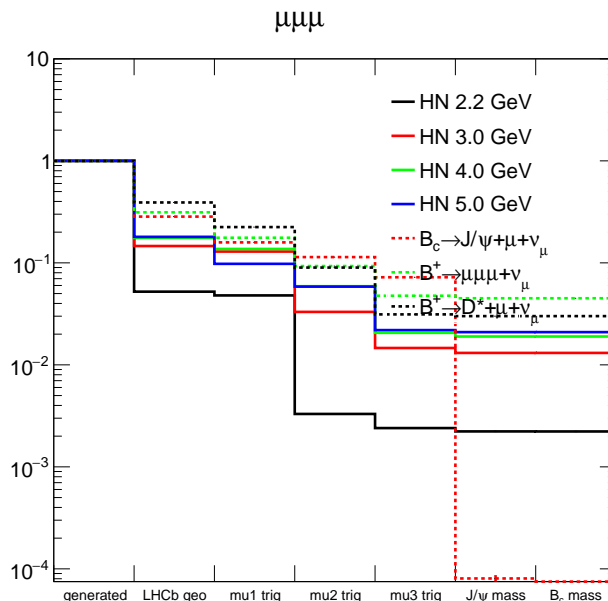


Figure 5.16: Efficiency of applying acceptance and signal selection cuts consecutively. The minimum  $p_T$  for muons to be triggered is assumed to be 1.3 GeV. Requiring the invariant mass of  $\mu_2^+$  and  $\mu_3^-$  to be outside of the 3.0-3.2 GeV window removes the  $J/\psi$  background.

We also show the effect of applying a 1.3 GeV trigger threshold on the  $p_T$  of each of the three muons, which demonstrates a high level of signal rejection in case of  $\mu_2^+$  for the low-mass candidate, due to the fact that the tau lepton has a mass close to this HN candidate and hence takes most of its energy in the decay, as also seen in figure 5.3.

### 5.5.2 $J/\psi$ background reduction

The effect of applying two generic signal selection criteria to reduce the  $J/\psi$  background is also shown in figure 5.16. Here, we have required the invariant mass of  $\mu_2^+$  and  $\mu_3^-$  to be outside of the 3.0-3.2 GeV window, which shows to remove almost completely the  $J/\psi$  background without affecting any of the other processes. It should be noted that in the final analysis using collision data, this selection will be affected by how much one can identify  $\mu_2^+$  compared to  $\mu_1^+$  with the same charge, but since the  $J/\psi$  peak is quite narrow, removing events with invariant mass within the  $J/\psi$  peak for both  $\mu_1^+-\mu_3^-$  and  $\mu_2^+-\mu_3^-$  pairs will not noticeably affect the signal acceptance.

### 5.5.3 Flight distance selections

The main efficiency study in this analysis concerns the selections based on flight distance. There are two types of such selections. In the search for HNs with higher couplings and lower  $c\tau$ , background rejection becomes very important, and a key selection is based on the flight distance between the production vertices of the muon pairs.

In the SM background processes, the highest flight distance comes from the  $D^*$  background due to the presence of D mesons. This process, which has the highest branching ratio among

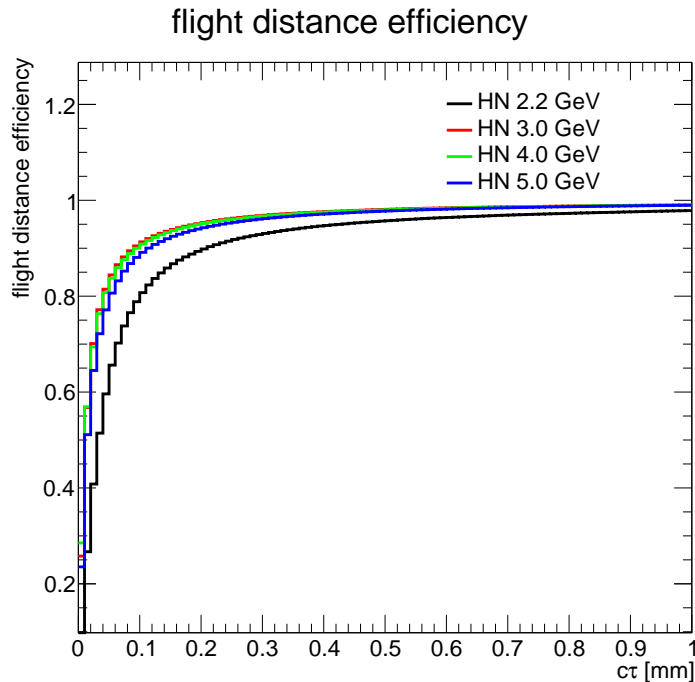


Figure 5.17: Efficiency of signal selection based on the flight distance to reject Standard Model background events, as a function of the proper flight distance  $c\tau$ .

the considered background processes, is expected to have flight distances of the order of a few hundred micrometers. A  $700 \mu\text{m}$  cut on the flight distance showed to remove all backgrounds.

To apply this selection, one has to take into account the resolution in the measurement of the flight distance. Experimentally, this resolution improves with a higher number of tracks from each vertex. According to figure 33 of reference [59], in processes with similar track multiplicity as our signature, an average resolution of  $150 \mu\text{m}$  on the vertex position in  $z$  is expected. Given that the production vertex of HN has only one visible track, one practically has to find the distance of closest approach between the decay vertex of HN and  $\mu_1^+$ , for which a resolution of  $350 \mu\text{m}$  seems realistic. In my current analysis, I have taken the true distance between the production vertices of  $\mu_1^+$  and  $\mu_3^-$  in each signal or background event, smeared it with a Gaussian distribution with a width of  $350 \mu\text{m}$ , and applied the  $700 \mu\text{m}$  lower threshold on it. In a more sophisticated analysis with fully reconstructed simulations and the collision data, usage of variables like distance of closest approach is recommended, since the production vertex of  $\mu_1^+$  is expected to have just a single track and hence not precisely reconstructible.

Figure 5.17 shows the efficiency of this selection for various signal candidates. For signal candidates with very small  $c\tau$ , addition of other selections especially on the  $\mu_2^+-\mu_3^-$  invariant mass is recommended, which completely removes the  $J/\psi$  and highly reduces the  $D^*$  background, but given that these HN candidates would have coupling values that are already excluded, this addition does not seem necessary.

In order to search for HNs with low coupling to leptons, lack of signal efficiency can arise from the limited size of the detector. In that regard, we need to apply an upper cut on the flight distance to ensure that the final-state muons can be reconstructed by LHCb. Although  $\mu_1^+$  is a decay product of the mother  $B_c^+$  and therefore reconstructable, the other two muons can decay much further. If a full tracking of  $\mu_2^+$  and  $\mu_3^-$  is required, an upper cut of 1 m on HN flight distance is suggested, as also used in reference [46]. However, as seen in figure 4.3, if these two muons are generated within 15 m of the interaction point, they will leave traces

in the muon system and hence detectable, even if their precise 4-momentum is not measured. Therefore, for HNs with a small flight distance, all three tracks will be in VELO, which is useful in identifying this signal against SM backgrounds. For HNs with flight distances of a few meters, the absence of precise tracks in VELO is acceptable, as the signature of two muon tracks with no corresponding VELO tracks is easily distinguished from the SM backgrounds.

In terms of triggering such highly displaced events and given the flexibility of the upgraded LHCb triggering system with no hardware tier, I suggest the development or usage of a targeted trigger which requires three muons, one with a track in the vertex locator and tracker layers, and two opposite-sign muon tracks in the muon system without explicit requirement on upstream tracks. This signature should be rare enough to remove online thresholds on the muon  $p_T$  and maximize signal acceptance.

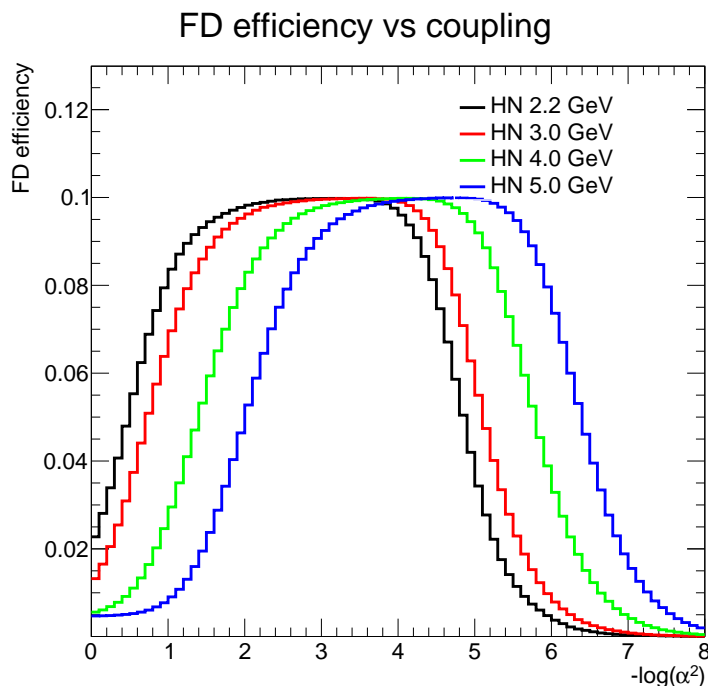


Figure 5.18: Efficiency of signal selection based on the flight distance as a function of  $-\log(\alpha^2)$ , with  $\alpha^2$  the coupling squared of a heavy neutrino and a muon. Lower limits on flight distance to reject background events affects the high-coupling region at the left tail, and a higher limit on flight distance to reject heavy neutrinos outside of the LHCb detection size affects the low-coupling region at the right tail.

To demonstrate the efficiency of the flight distance requirement both in the low- $c\tau$  and high- $c\tau$  regions, one can convert  $c\tau$  to a corresponding coupling. This will be useful later in extracting the reach of LHCb sensitivity region in terms of coupling. Figure 5.18 shows the efficiency as a function of  $-\log(\alpha^2)$ , with  $\alpha^2$  the squared coupling of a HN and a muon. In the conversion between  $c\tau$  and  $\alpha^2$ , the coupling of the HN to the other two leptons is set to zero for simplicity. This conversion is adapted from a script provided by the authors of reference [46], which provides  $c\tau$  as a function of the HN mass and coupling to each of the three leptons. From figure 5.18, it can be seen that for  $\alpha^2 > 10^{-2}$  the background rejection selection reduces the sensitivity, and for small couplings  $\alpha^2 < 10^{-5}$  the limited size of the detector is the main constraint in this search.

## 5.6 Results

Following an evaluation of acceptance and efficiency of signal selection as a function of HN coupling in the previous section, and using the theoretical relation between the coupling, mass, and branching ratio, one can estimate the number of HN events recorded by LHCb per year, which is the final deliverable of my analysis.

In terms of branching ratios, I have developed an automated script to calculate the branching ratio and decay width based on the theoretical calculations of reference [46] and as a function of the mass and coupling of the HNs. For simplicity in demonstrating the effect of efficiency and acceptance, I first show results for the LNV process in subsection 5.6.1, assuming a coupling of zero between the HN and both electron and tau lepton. The final results allowing freely floating couplings to muon and tau, with no coupling to electron will be shown in subsection 5.6.2.

### 5.6.1 Lepton number violating process

To clarify the contributing factors in the sensitivity of the HN search, I start by the assumption that the HN only couples to muon, hence allowing only the LNV process with a full suppression of the LNC process. Therefore, I will for now only focus on the Majorana HNs.

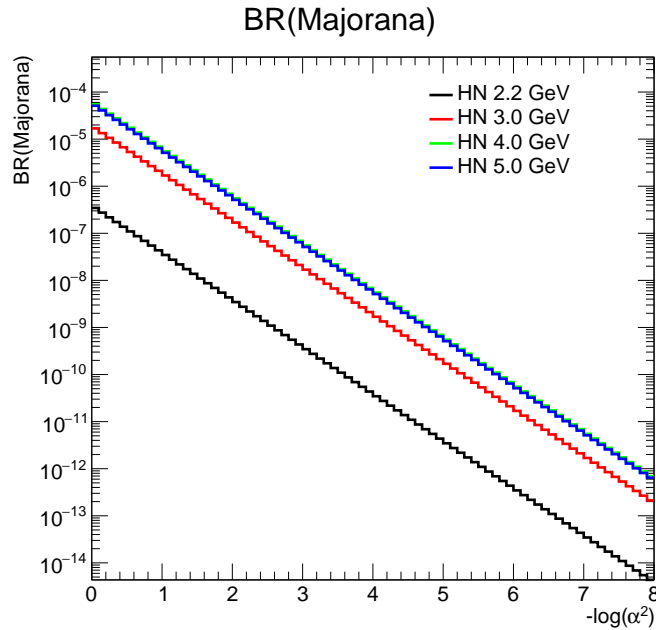


Figure 5.19: Branching ratio (BR) of a Majorana signal candidate in a lepton number violating decay of  $B_c^+$  meson as a function of  $-\log(\alpha^2)$ , with  $\alpha^2$  the squared coupling of a heavy neutrino and a muon.

Figure 5.19 shows the results of the theoretical calculations. For each mass, and given that in the LNV process we are only sensitive to coupling to muons, the branching ratio is a function of the muon  $\alpha^2$ . This is because in this scenario with only one lepton, the decay of HN to muon has a 100% probability and therefore the coupling only plays a role in the production vertex of the HN.

In terms of efficiency and acceptance, it can be inferred from the previous discussions that the main selections are on the flight distance and geometrical acceptance. Kinematic background rejections such as the use of invariant mass of dimuons or their opening azimuthal angle were studied and evaluated, but they will be more relevant for highly coupled HNs with small  $c\tau$ ,

which are currently excluded by other experiments. Moreover, a trigger algorithm based on highly displaced muon pairs and a third muon matched with a track in VELO is proposed, for which the efficiency can be assumed to be close to unity due to the rareness of this signature.

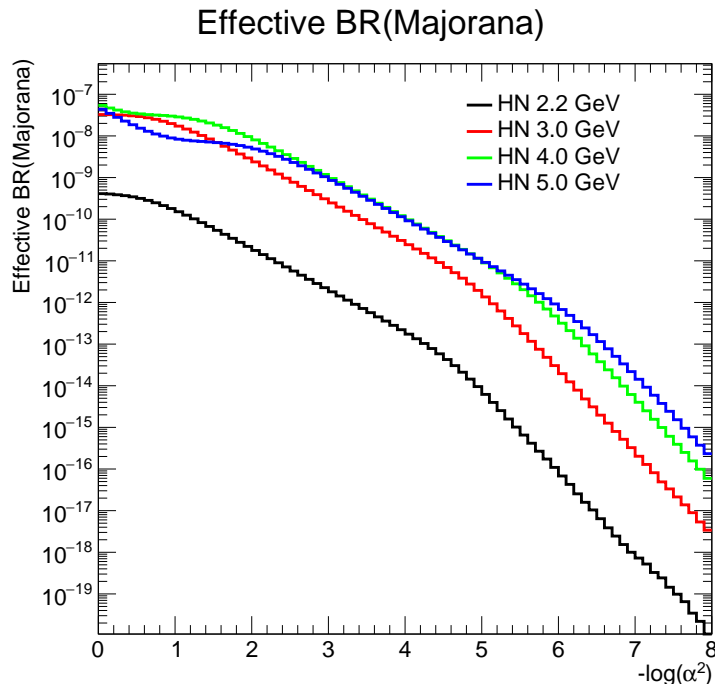


Figure 5.20: Effective branching ratio (BR) of a Majorana signal candidate in a lepton number violating decay of  $B_c^+$  meson as a function of  $-\log(\alpha^2)$ , with  $\alpha^2$  the squared coupling of a heavy neutrino to a muon. The theoretical branching ratio has been multiplied by efficiency and acceptance factors found in this analysis.

Figure 5.20 shows the effective branching ratio after applying the geometrical acceptance of the LHCb detector and the efficiency of the upper and lower cuts on the flight distance of the HN, measured as the distance between the production vertices of  $\mu_1^+$  and  $\mu_3^-$ .

Compared with the values of the branching ratio reported in [46] for a specific coupling and two mass points, we see differences that are rooted in three main factors. Firstly, in this analysis I apply realistic geometrical requirements on the final-state particles to be within the acceptance region of the LHCb detector both upstream and downstream, while in reference [46] a full  $4\pi$  detector was assumed which highly overestimates the acceptance. Secondly, the acceptance factor in reference [46] is not event-by-event and requires the HN to decay within  $1\text{ m}$  of the interaction point to stay within VELO, while my proposed analysis approach allows highly displaced muon pairs as long as they are generated before the muon system, enlarging the acceptance region for this analysis, especially in the more critical region of phase space with lower couplings and larger  $c\tau$ . Thirdly, in reference [46] no branching ratio factor is applied for the decay of the tau lepton, while in this analysis a branching fraction of 17.39% for the decay of tau to muon and two neutrinos is taken into account. Overall, I observe that the efficiency and acceptance factors used in reference [46] are about an order of magnitude overestimated.

With an instantaneous luminosity of  $10^{34}\text{ cm}^{-2}\text{ s}^{-1}$  during HL-LHC, about  $5 \times 10^{10}$   $B_c$  mesons are expected to be produced at the LHCb collision point in each year [60]. Having the full effective branching ratios of the  $B_c^+$  decays shown in figure 5.1, and assuming that the HN only decays to muons, one can find the expected number of Majorana HNs recorded per year during the HL-LHC era. These numbers are shown for various mass points in figure 5.21 as a function

of  $-\log(\alpha^2)$ , with  $\alpha^2$  the squared coupling of a HN to a muon.

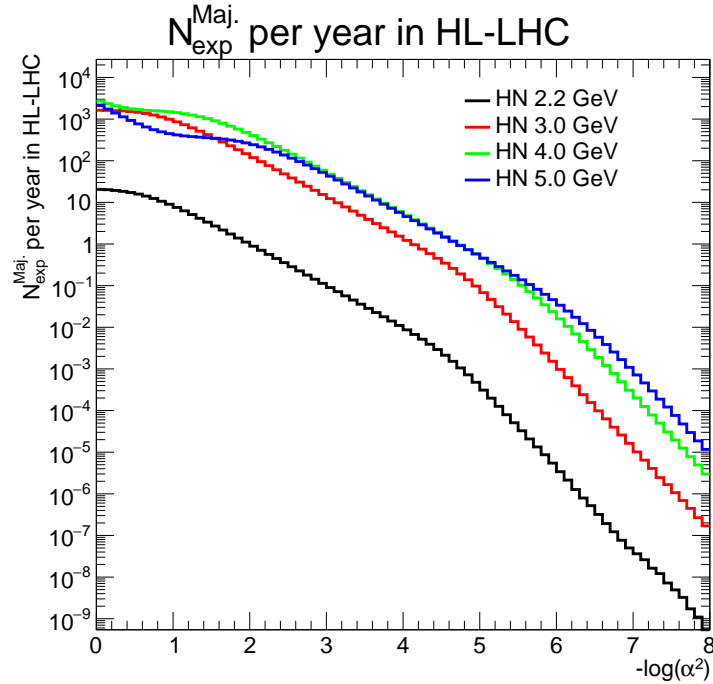


Figure 5.21: Expected number of Majorana heavy neutrinos for various assumptions on the heavy neutrino mass, for a Majorana signal candidate in a lepton number violating decay of  $B_c$  meson and as a function of  $-\log(\alpha^2)$ , with  $\alpha^2$  the squared coupling or mixing element of a heavy neutrino and a muon. Couplings of heavy neutrino to electron and tau lepton are set to zero for simplicity.

### 5.6.2 Sensitivity to Majorana and Dirac heavy neutrinos

After understanding the effect of geometrical acceptance and signal selection on the sensitivity, I now present the final result of this analysis, with as realistic assumptions as possible given the scope of this study. Similarly to the LNV results, I calculated the branching ratios and decay widths as a function of the HN mass and coupling, this time to both muon and tau leptons. The decay width is used to calculate the efficiency of selections based on the flight distance.

Figure 5.22 shows the theoretical branching ratio of the  $B_c$  decays to a Majorana HN, followed by the LNV or LNC process to get three muon final states and corrected with the branching ratio of tau decay into a muon and two neutrinos. The branching ratio is plotted as a function of the squared coupling or mixing element of the HN and the muon and tau lepton for five HN mass points of 2.2, 3.0, 4.0, 4.5, and 5.0 GeV. It can be seen that for a Majorana HN, the dependence on the tau coupling is much weaker than that of the muon, leading to similar results shown for the LNV process with no tau coupling.

Figure 5.23 shows the same branching ratio, this time for the Dirac HNs and therefore only through the LNC process. Since in the LNC process the HN shares a production vertex with a muon and a decay vertex with a tau lepton, its branching ratio depends on  $\alpha_\mu^2 \alpha_\tau^2$  divided by its decay width which is a weighted quadratic sum of the two  $\alpha^2$  values. As a result, the dependence on these two couplings is rather symmetric as also seen in this figure.

Finally, after applying the geometric acceptance and signal selection efficiency based on  $c\tau$ , and using the estimation [60] that during HL-LHC, about  $5 \times 10^{10}$   $B_c$  mesons are produced per year

at the LHCb interaction point, I obtain the expected number of HN candidates observed by the LHCb experiment in each year. These numbers are shown for five HN candidates of 2.2, 3.0, 4.0, 4.5, and 5.0 GeV in figure 5.24 for the Majorana case and figure 5.25 for the Dirac HN candidates. It can be inferred that the 4-5 GeV mass range has the most sensitivity in this analysis. The current best exclusion limit on the coupling squared to muons in this HN mass range is  $10^{-6}$ , set by a recent CMS analysis [28]. Therefore, this analysis predicts a maximum of 0.1 recorded events per year, for the specific decay channel of  $B_c^+ \rightarrow \mu^+ \text{HN} \rightarrow \mu^+ \mu^+ \tau^- \bar{\nu}_\tau \rightarrow \mu^+ \mu^+ \mu^- \bar{\nu}_\mu \nu_\tau \bar{\nu}_\tau$  and its charge conjugate, which is too low for an observation of the process or improvement of the exclusion limits during Run3 and Run4 of LHC.

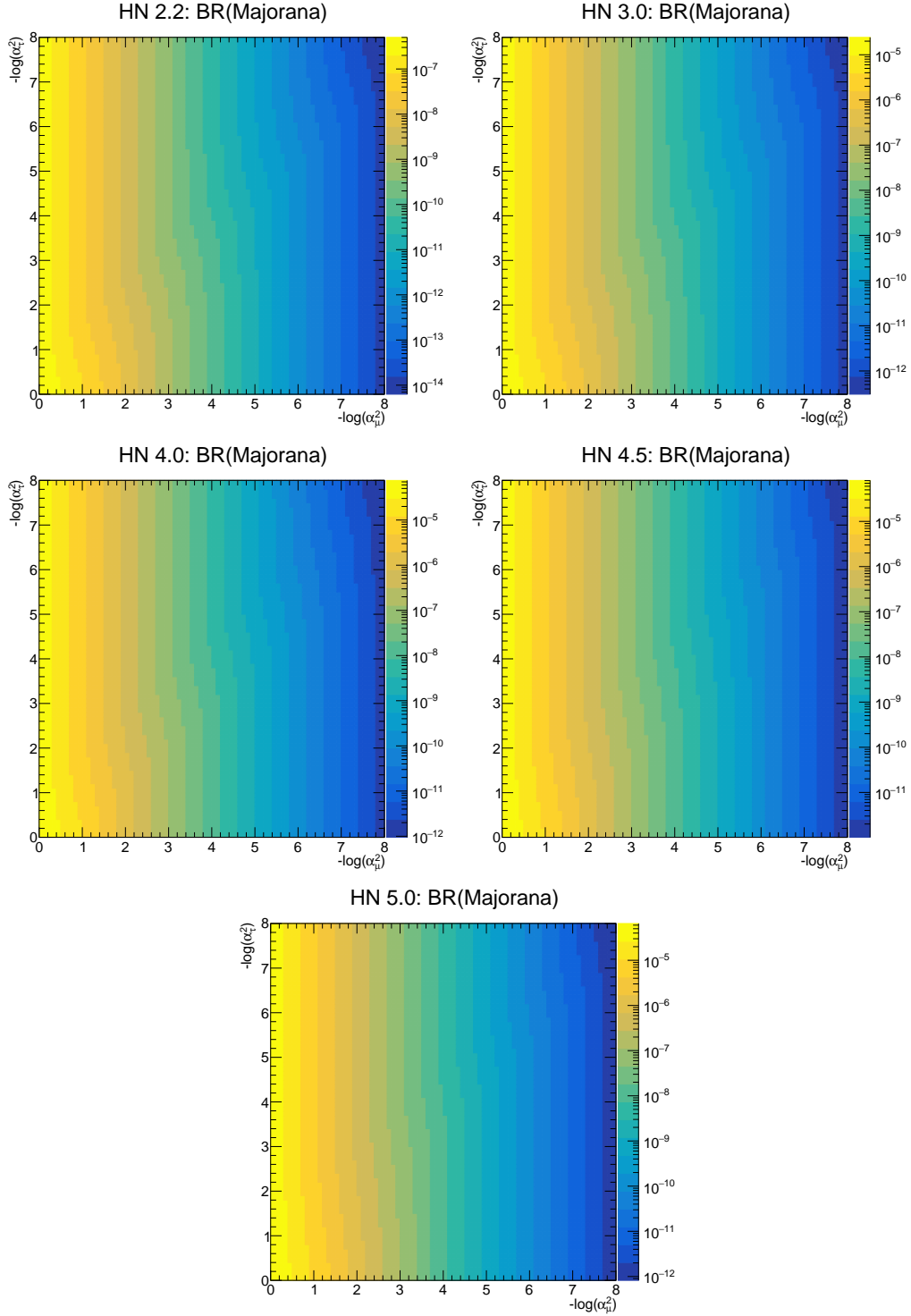


Figure 5.22: Branching ratio of Majorana heavy neutrinos in both lepton number violating and lepton number conserving decays of  $B_c$  meson as a function of  $-\log(\alpha_\ell^2)$ , with  $\alpha_\ell^2$  ( $\ell = \mu, \tau$ ) the squared coupling or mixing element of a heavy neutrino and a muon or a tau lepton. Five heavy neutrino mass points of 2.2, 3.0, 4.0, 4.5, and 5.0 GeV are shown.

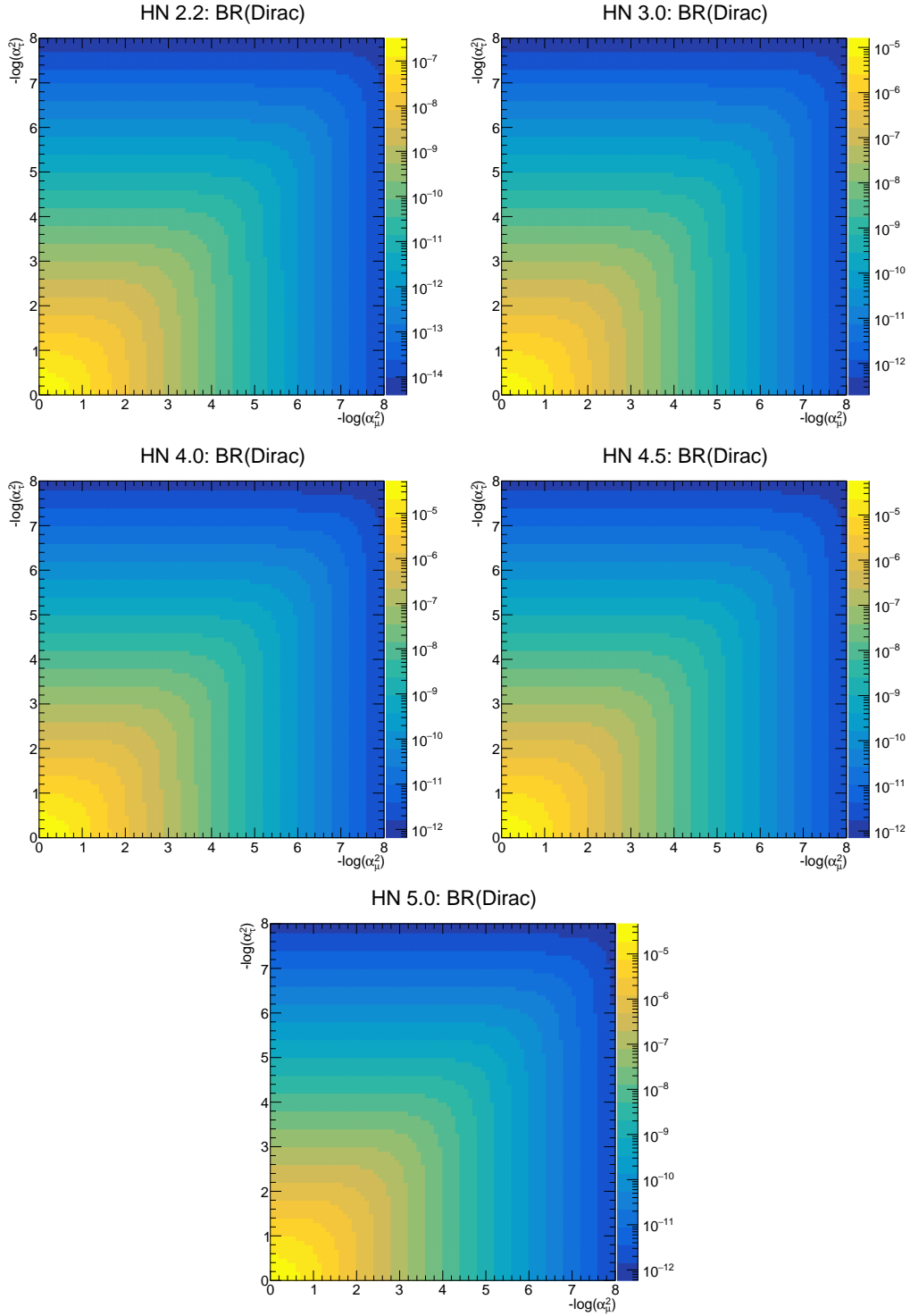


Figure 5.23: Branching ratio of Dirac heavy neutrinos in the lepton number conserving decays of  $B_c$  meson as a function of  $-\log(\alpha_\ell^2)$ , with  $\alpha_\ell^2$  ( $\ell = \mu, \tau$ ) the squared coupling or mixing element of a heavy neutrino and a muon or a tau lepton. Five heavy neutrino mass points of 2.2, 3.0, 4.0, 4.5, and 5.0 GeV are shown.

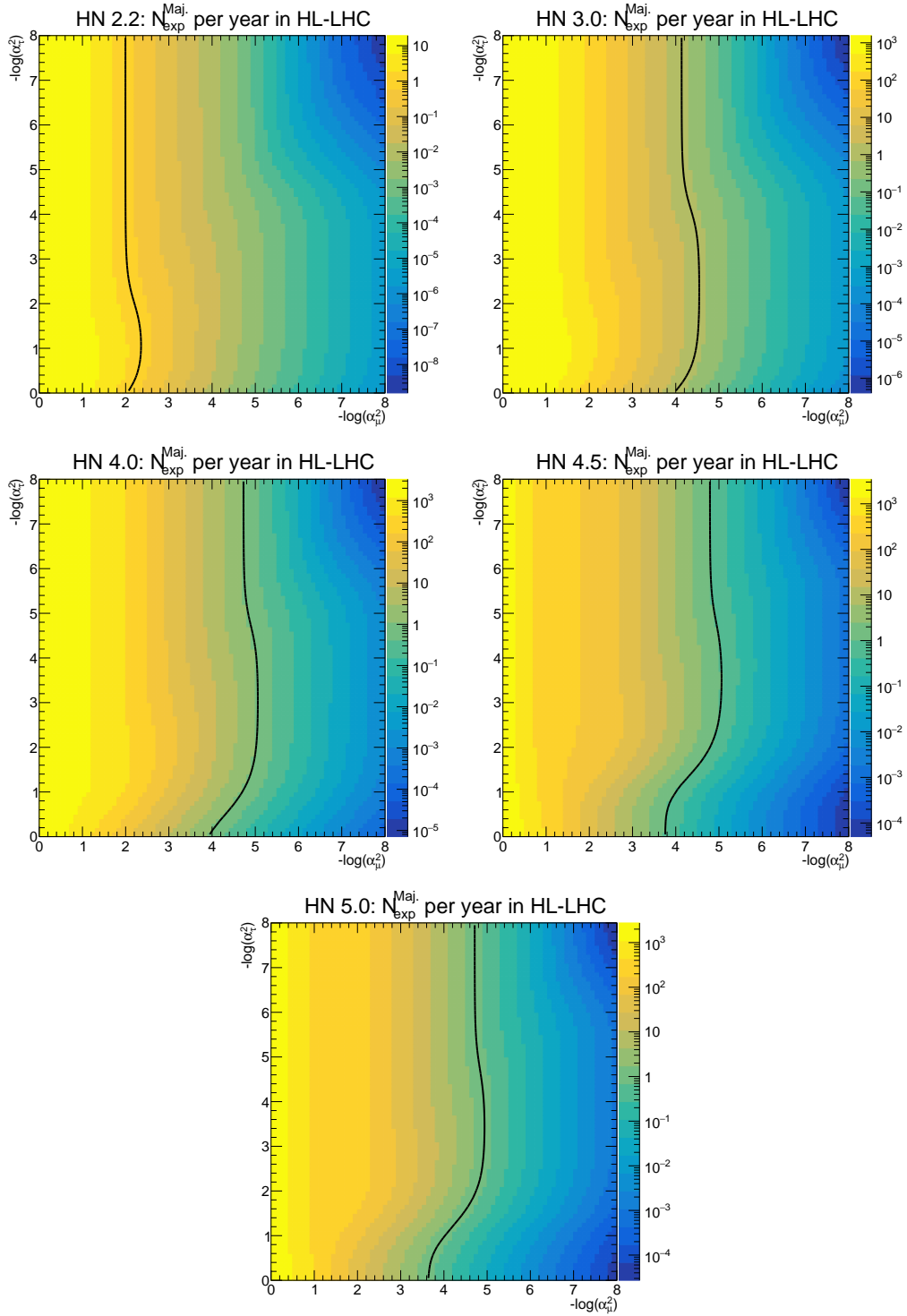


Figure 5.24: Expected number of Majorana heavy neutrinos per year in both lepton number violating and lepton number conserving decays of  $B_c$  meson as a function of  $-\log(\alpha_\ell^2)$ , with  $\alpha_\ell^2$  ( $\ell = \mu, \tau$ ) the squared coupling or mixing element of a heavy neutrino and a muon or a tau lepton. Five heavy neutrino mass points of 2.2, 3.0, 4.0, 4.5, and 5.0 GeV are shown. Solid black lines show the contour of 1.0 expected event.

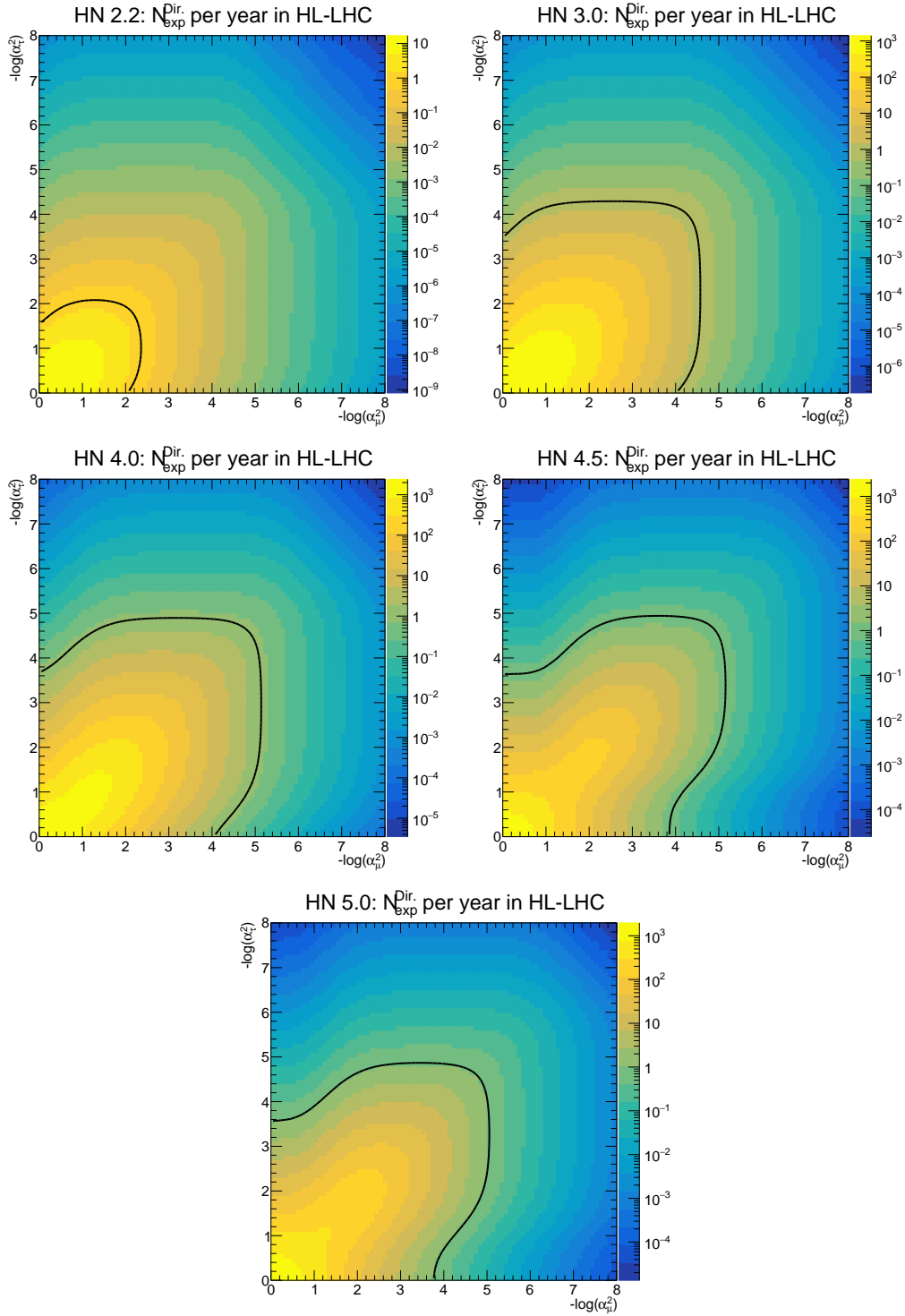


Figure 5.25: Expected number of Dirac heavy neutrinos per year in lepton number conserving decays of  $B_c$  meson as a function of  $-\log(\alpha_\ell^2)$ , with  $\alpha_\ell^2$  ( $\ell = \mu, \tau$ ) the squared coupling or mixing element of a heavy neutrino and a muon or a tau lepton. Five heavy neutrino mass points of 2.2, 3.0, 4.0, 4.5, and 5.0 GeV are shown. Solid black lines show the contour of 1.0 expected event.

## 6 Summary and conclusion

In this thesis, I present a study to estimate the sensitivity of the LHCb experiment in searches for heavy neutrinos. I started by a generic review of the Standard Model in chapter 2, as the most successful theory in hand to describe the building blocks of the universe and their interactions. In chapter 3, I discussed the shortcomings of this theory and the motivation for particular beyond-Standard-Model particles called heavy neutrinos. I presented a review on the theoretical and experimental status of heavy neutrino studies, focusing on specific candidates that could be observed in the decays of the  $B_c$  mesons at the LHCb experiment.

After a short review of the LHC accelerator and the LHCb experiment in chapter 4, an analysis was presented in chapter 5 to estimate the reach of the LHCb in the proposed [46] decay channel of  $B_c^+ \rightarrow \mu^+ \text{HN} \rightarrow \mu^+ \mu^+ \tau^- \bar{\nu}_\tau \rightarrow \mu^+ \mu^+ \mu^- \bar{\nu}_\mu \nu_\tau \bar{\nu}_\tau$  and its charge conjugate. Even though the choice of a tau lepton compared to other flavors results in an overall lower branching ratio after the tau decay, it was motivated by a kinematic advantage to distinguish between Majorana and Dirac heavy neutrinos if sufficient number of heavy neutrinos could be observed. In this project, signal and background processes were simulated in order to develop a set of signal selection criteria and estimate the efficiency and acceptance of the heavy neutrino signal as a function of its mass, coupling to leptons, and its Majorana or Dirac nature. I proposed an online triggering strategy which targets the specific signature of these heavy neutrino events, and hence will have an efficiency close to one. These results eventually led to estimations on the number of events observed by the LHCb experiment per year during Run3 and Run4 of LHC. These results, shown in figure 5.24 for Majorana and in figure 5.25 for Dirac heavy neutrinos, show the potential of such a heavy neutrino search for various coupling and mass assumptions.

In short, my analysis concludes that this search is the most sensitive for heavy neutrino masses around 4-5 GeV, but given the recent exclusion limits on the coupling of heavy neutrino to muons from the CMS experiment [28] at this mass, LHCb can expect a maximum of 0.1 such events per year during Run3 and Run4 of LHC, which is statistically insufficient. This number is smaller than the previous estimate in reference [46] and shown in table 3.1, which is mainly a result of accounting for geometrical acceptance of the LHCb detector and a corrected estimation of the branching ratios.

# Bibliography

- [1] Wikimedia Commons, “File:standard model of elementary particles.svg — wikimedia commons, the free media repository,” 2023. (Retrieved Jan 13, 2023).
- [2] Y. Fukuda *et al.*, “Evidence for oscillation of atmospheric neutrinos,” *Phys. Rev. Lett.*, vol. 81, pp. 1562–1567, Aug 1998.
- [3] SNO Collaboration, “Direct Evidence for Neutrino Flavor Transformation from Neutral-Current Interactions in the Sudbury Neutrino Observatory,” *Phys. Rev. Lett.*, vol. 89, p. 011301, Jun 2002.
- [4] KamLAND Collaboration, “First Results from KamLAND: Evidence for Reactor Antineutrino Disappearance,” *Phys. Rev. Lett.*, vol. 90, p. 021802, Jan 2003.
- [5] D. J. Griffiths, *Introduction to elementary particles; 2nd rev. version*, ch. 12. Physics textbook, New York, NY: Wiley, 2008.
- [6] A. M. Abdullahi *et al.*, “The present and future status of heavy neutral leptons,” *Journal of Physics G: Nuclear and Particle Physics*, vol. 50, p. 020501, Jan 2023.
- [7] L. Edelhäuser and A. Knochel, *Tutorium Quantenfeldtheorie*, ch. 12. Springer Spektrum, 2016.
- [8] I. Esteban, M. Gonzalez-Garcia, M. Maltoni, T. Schwetz-Mangold, and A. Zhou, “The fate of hints: updated global analysis of three-flavor neutrino oscillations,” *Journal of High Energy Physics*, vol. 2020, 09 2020.
- [9] S. R. Choudhury and S. Hannestad, “Updated results on neutrino mass and mass hierarchy from cosmology with planck 2018 likelihoods,” *Journal of Cosmology and Astroparticle Physics*, vol. 2020, p. 037, jul 2020.
- [10] S. R. Choudhury and S. Hannestad, “Updated results on neutrino mass and mass hierarchy from cosmology with planck 2018 likelihoods,” *Journal of Cosmology and Astroparticle Physics*, vol. 2020, p. 037, jul 2020.
- [11] J. A. Formaggio, A. L. C. de Gouvêa, and R. H. Robertson, “Direct measurements of neutrino mass,” *Physics Reports*, vol. 914, pp. 1–54, 2021. Direct measurements of neutrino mass.
- [12] P. Minkowski, “ $\mu \rightarrow e\gamma$  at a rate of one out of  $10^9$  muon decays?,” *Physics Letters B*, vol. 67, no. 4, pp. 421–428, 1977.
- [13] M. Gell-Mann, P. Ramond, and R. Slansky, “Complex spinors and unified theories,” in *Supergravity Workshop* (D. Freedman and P. van Nieuwenhuizen, eds.), (Amsterdam, NL), pp. 315–321, North Holland, 1979.
- [14] R. N. Mohapatra and G. Senjanović, “Neutrino mass and spontaneous parity nonconservation,” *Phys. Rev. Lett.*, vol. 44, pp. 912–915, Apr 1980.

- [15] T. Yanagida, “Horizontal gauge symmetry and masses of neutrinos,” in *Proceedings of the Workshop on Unified Theories and Baryon Number in the Universe*, (Tsukuba, Japan), pp. 95–99, 1979.
- [16] J. Schechter and J. W. F. Valle, “Neutrino masses in  $su(2) \otimes u(1)$  theories,” *Phys. Rev. D*, vol. 22, pp. 2227–2235, Nov 1980.
- [17] S. Dodelson and L. M. Widrow, “Sterile neutrinos as dark matter,” *Phys. Rev. Lett.*, vol. 72, pp. 17–20, Jan 1994.
- [18] A. Boyarsky, M. Drewes, T. Lasserre, S. Mertens, and O. Ruchayskiy, “Sterile neutrino dark matter,” *Progress in Particle and Nuclear Physics*, vol. 104, pp. 1–45, 2019.
- [19] M. Fukugita and T. Yanagida, “Baryogenesis without grand unification,” *Physics Letters B*, vol. 174, no. 1, pp. 45–47, 1986.
- [20] T. Asaka, S. Blanchet, and M. Shaposhnikov, “The  $\nu$ msm, dark matter and neutrino masses,” *Physics Letters B*, vol. 631, no. 4, pp. 151–156, 2005.
- [21] T. Asaka and M. Shaposhnikov, “The  $\nu$ msm, dark matter and baryon asymmetry of the universe,” *Physics Letters B*, vol. 620, no. 1, pp. 17–26, 2005.
- [22] P. D. Bolton, F. F. Deppisch, and P. S. Bhupal Dev, “Neutrinoless double beta decay versus other probes of heavy sterile neutrinos,” *JHEP*, vol. 03, p. 170, 2020.
- [23] O. Adriani *et al.*, “Search for isosinglet neutral heavy leptons in  $Z^0$  decays,” *Phys. Lett. B*, vol. 295, pp. 371–382, 1992.
- [24] P. Achard *et al.*, “Search for heavy isosinglet neutrino in  $e^+e^-$  annihilation at lep,” *Physics Letters B*, vol. 517, pp. 67–74, 07 2001.
- [25] P. Abreu, W. Adam, T. Adye, I. Azhinenko, G. Alekseev, R. Alemany, P. Allport, S. Almed, U. Amaldi, S. Amato, A. Andreazza, M. Andrieux, P. Antilogus, W. Apel, B. Asman, J. Augustin, A. Augustinus, P. Baillon, P. Bambade, and G. Zumerle, “Search for neutral heavy leptons produced in  $z$  decays,” *Zeitschrift fur Physik C-Particles and Fields*, vol. 74, 03 1997.
- [26] A. Sirunyan *et al.*, “Search for Heavy Neutral Leptons in Events with Three Charged Leptons in Proton-Proton Collisions at  $\sqrt{s} = 13$  TeV,” *Physical Review Letters*, vol. 120, 02 2018.
- [27] A. M. Sirunyan *et al.*, “Search for heavy Majorana neutrinos in same-sign dilepton channels in proton-proton collisions at  $\sqrt{s} = 13$  TeV,” *JHEP*, vol. 01, p. 122, 2019.
- [28] A. Tumasyan *et al.*, “Search for long-lived heavy neutral leptons with displaced vertices in proton-proton collisions at  $\sqrt{s} = 13$  TeV,” *JHEP*, vol. 07, p. 081, 2022.
- [29] A. Hayrapetyan *et al.*, “Search for long-lived heavy neutral leptons with lepton flavour conserving or violating decays to a jet and a charged lepton,” *Journal of High Energy Physics*, vol. 2024, p. 105, Mar 2024.
- [30] A. Hayrapetyan *et al.*, “Search for long-lived heavy neutral leptons decaying in the CMS muon detectors in proton-proton collisions at  $\sqrt{s} = 13$  TeV,” *Phys. Rev. D*, vol. 110, p. 012004, Jul 2024.

- [31] G. Aad *et al.*, “Search for heavy Majorana neutrinos with the ATLAS detector in pp collisions at  $\sqrt{s} = 8$  TeV,” *JHEP*, vol. 07, p. 162, 2015.
- [32] G. Aad *et al.*, “Search for heavy neutral leptons in decays of W bosons produced in 13 TeV pp collisions using prompt and displaced signatures with the ATLAS detector,” *Journal of High Energy Physics*, vol. 2019, 10 2019.
- [33] G. Aad *et al.*, “Search for Heavy Neutral Leptons in Decays of W Bosons Using a Dilepton Displaced Vertex in  $\sqrt{s} = 13$  TeV pp Collisions with the ATLAS Detector,” *Phys. Rev. Lett.*, vol. 131, p. 061803, Aug 2023.
- [34] LHCb Collaboration, “Search for heavy neutral leptons in  $W^+ \rightarrow \mu^+ \mu^\pm$  jet decays,” *The European Physical Journal C*, vol. 81, p. 248, Mar 2021.
- [35] M. Aoki, M. Blecher, D. A. Bryman, S. Chen, M. Ding, L. Doria, P. Gumplinger, C. Hurst, A. Hussein, Y. Igarashi, N. Ito, S. H. Kettell, L. Kurchaninov, L. Littenberg, C. Malbrunot, T. Numao, R. Poutissou, A. Sher, T. Sullivan, D. Vavilov, K. Yamada, and M. Yoshida, “Search for massive neutrinos in the decay  $\pi \rightarrow e\nu$ ,” *Phys. Rev. D*, vol. 84, p. 052002, Sep 2011.
- [36] E. Cortina Gil *et al.*, “Search for heavy neutral lepton production in  $k^+$  decays,” *Physics Letters B*, vol. 778, pp. 137–145, 2018.
- [37] D. Liventsev, I. Adachi, H. Aihara, K. Arinstein, D. Asner, V. Aulchenko, T. Aushev, A. Bakich, A. Bay, K. Belous, B. Bhuyan, A. Bondar, G. Bonvicini, A. Bozek, M. Bracko, T. Browder, P. Chang, V. Chekelian, A. Chen, and A. Zupanc, “Search for heavy neutrinos at belle,” *Physical Review D*, vol. 87, 01 2013.
- [38] J. Badier *et al.*, “Mass and lifetime limits on new longlived particles in 300-gev/c  $\pi^-$  interactions,” *Zeitschrift für Physik C*, vol. 31, p. 21, 1986.
- [39] J. Dorenbosch *et al.*, “A search for decays of heavy neutrinos in the mass range 0.5–2.8 gev,” *Physics Letters B*, vol. 166, no. 4, pp. 473–478, 1986.
- [40] P. Vilain *et al.*, “Search for heavy isosinglet neutrinos,” *Physics Letters B*, vol. 343, pp. 453–458, 1995. [Phys. Lett. B351, 387 (1995)].
- [41] G. Bernardi, G. Carugno, J. Chauveau, F. Dicarolo, M. Dris, J. Dumarchez, M. Ferro-Luzzi, J.-M. Levy, D. Lukas, J.-M. Perreau, Y. Pons, A.-M. Touchard, and F. Vannucci, “Further limits on heavy neutrino couplings,” *Physics Letters B*, vol. 203, no. 3, pp. 332–334, 1988.
- [42] The LHCb Collaboration, “Search for Majorana Neutrinos in  $B^- \rightarrow \pi^+ \mu^- \mu^-$  Decays,” *Phys. Rev. Lett.*, vol. 112, p. 131802, Apr 2014.
- [43] A. T. C. c. Hayrapetyan, “Search for long-lived heavy neutrinos in the decays of B mesons produced in proton-proton collisions at  $\sqrt{s} = 13$  TeV,” *Journal of High Energy Physics*, vol. 2024, p. 183, Jun 2024.
- [44] A. Atre, T. Han, S. Pascoli, and B. Zhang, “The search for heavy majorana neutrinos,” *Journal of High Energy Physics*, vol. 2009, p. 030, May 2009.
- [45] B. Shuve and M. E. Peskin, “Revision of the LHCb limit on Majorana neutrinos,” *Phys. Rev. D*, vol. 94, p. 113007, Dec 2016.

- [46] G. A. Vasquez and J. Zamora-Saa, “Unveiling the heavy neutrino nature at LHCb,” *Phys. Rev. D*, vol. 108, p. 053008, Sep 2023.
- [47] G. Cvetic, C. S. Kim, and J. Zamora-Saa, “ $cp$  violation in lepton number violating semi-hadronic decays of  $k, d, D_s, b, B_c$ ,” *Phys. Rev. D*, vol. 89, p. 093012, May 2014.
- [48] G. Cvetic, C. Dib, C. Kim, and J. Zamora-Saa, “Probing majorana neutrinos and their  $cp$  violation in decays of charged scalar mesons  $\pi, k, d, ds, b, bc$ ,” *Symmetry*, vol. 7, 03 2015.
- [49] G. Cvetic, C. Dib, and C. Kim, “Probing majorana neutrinos in rare  $\pi^+ \rightarrow e^+e^+\mu^-\nu$  decays,” *Journal of High Energy Physics*, vol. 2012, 06 2012.
- [50] I. Boiarska, A. Boyarsky, O. Mikulenko, and M. Ovchinnikov, “Constraints from the charm experiment on heavy neutral leptons with tau mixing,” *Phys. Rev. D*, vol. 104, p. 095019, Nov 2021.
- [51] The LHCb collaboration, “Measurement of the track reconstruction efficiency at LHCb,” *Journal of Instrumentation*, vol. 10, p. P02007, Feb 2015.
- [52] I. Gouz, V. Kiselev, A. Likhoded, V. Romanovsky, and O. Yushchenko, “Prospects for the  $B_c$  studies at LHCb,” *Physics of Atomic Nuclei - PHYS ATOM NUCL-ENGL TR*, vol. 67, pp. 1559–1570, 08 2004.
- [53] L. Forthomme (Wikimedia Commons), “File:cern-accelerator-complex.svg — wikimedia commons, the free media repository,” 2016. (Retrieved Jul 24, 2017).
- [54] “LHC long term schedule.” (Retrieved Dec 04, 2024).
- [55] The LHCb Collaboration, “The LHCb Detector at the LHC,” *Journal of Instrumentation*, vol. 3, p. S08005, aug 2008.
- [56] R. Aaij *et al.*, “The LHCb Upgrade I,” *JINST*, vol. 19, no. 05, p. P05065, 2024.
- [57] F. Archilli *et al.*, “Performance of the Muon Identification at LHCb,” *Journal of Instrumentation*, vol. 8, p. P10020, oct 2013.
- [58] G. Cowan, D. Craik, and M. Needham, “Rapidsim: An application for the fast simulation of heavy-quark hadron decays,” *Computer Physics Communications*, vol. 214, pp. 239–246, 2017.
- [59] L. Collaboration, “LHCb VELO Upgrade Technical Design Report,” tech. rep., LHCb, 2013.
- [60] I. P. Gouz, V. V. Kiselev, A. K. Likhoded, V. I. Romanovsky, and O. P. Yushchenko, “Prospects for the  $B_c$  studies at LHCb,” *Physics of Atomic Nuclei*, vol. 67, pp. 1559–1570, Aug 2004.